Influence of ENSO and MJO on the zonal structure of tropical tropopause inversion layer using high-resolution temperature profiles retrieved from COSMIC GPS Radio Occultation

Noersomadi Noersomadi[1,2], Toshitaka Tsuda[1], Masatomo Fujiwara[3]

5 [1]Research Institute for Sustainable Humanosphere (RISH), Kyoto University, Uji, 611-0011, Japan
[2]National Institute of Aeronautics and Space (LAPAN), Bandung, 40173, Indonesia
[3]Faculty of Environmental Earth Science, Hokkaido University, Sapporo, 060-0810, Japan

Correspondence to: Noersomadi (noersomadi@lapan.go.id)

Abstract. Using COSMIC GPS Radio Occultation (RO) observations from January 2007 to December 2016, we retrieved
10 temperature profiles with the height resolution of about 0.1 km in the upper troposphere and lower stratosphere (UTLS). We investigated the distribution of static stability (N^2) and the zonal structure of the tropopause inversion layer (TIL) in the tropics, where a large change in temperature gradient occurs associated with sharp variations of N^2. We show the variations of the mean N^2 profiles in coordinates relative to the Cold Point Tropopause (CPT). A very thin (<1 km) layer is found with average maximum N^2 in the range of $11.0–12.0 \times 10^{-4}$ s^{-2}. The mean and standard deviation of TIL sharpness, defined as the
15 difference between the maximum N^2 ($maxN^2$) and minimum N^2 ($minN^2$) within ±1 km of the CPT, is $(10.5 \pm 3.7) \times 10^{-4}$ s^{-2}. The $maxN^2$ is typically located within 0.5 km above CPT.

We focused on the variation of TIL sharpness in two longitude regions, 90°–150°E (Maritime Continent; MC) and 170°–230°E (Pacific Ocean; PO), with different land–sea distribution. Seasonal variations of TIL sharpness and thickness were related to the deep convective activity represented by low Outgoing Longwave Radiation (OLR) during the Australian
20 and Asian monsoons. The deviation from the mean sharpness (sharpness anomaly) was out-of-phase with the OLR anomaly in both the MC and PO. The correlation between sharpness anomaly over the MC and PO and the sea surface temperature (SST) Niño 3.4 index was –0.66 and +0.88, respectively. During La Niña (SST Niño 3.4 < –0.5 K) in the MC, and El Niño (SST Niño 3.4 > +0.5 K) in the PO, warmer SSTs in the MC and PO produce more active deep convection that tends to force the air upward to the tropopause layer and increase the temperature gradient there. The intra-seasonal variation in sharpness
25 anomaly during slow and fast episodes of the Madden–Julian Oscillation (MJO) demonstrates that eastward propagation of positive sharpness anomaly is associated with organized deep convection. Deep convection during MJO will tend to decrease N^2 below CPT and increase N^2 above CPT thus enlarge the TIL sharpness. Convective activity in the tropics is a major control on variations in tropopause sharpness at intra-seasonal to interannual time-scales.

Keywords: COSMIC GPS-RO, tropopause inversion layer, tropics

1 Introduction

The tropical tropopause layer (TTL) at a height of 12–19 km plays an important role in the Earth's climate, as tropospheric air enters the stratosphere mainly in this region, where Stratosphere–Troposphere Exchange (STE) processes occur (Holton et al., 1995). The dynamics and radiative processes in the TTL have received much attention in the decades since the first observation of a slow meridional circulation, the Brewer–Dobson circulation (e.g., Butchart, 2014). In the tropics, the tropopause is defined as either the lapse rate tropopause (LRT) or the cold point tropopause (CPT). Here, the LRT refers to "the lowest level where the temperature lapse rate decreases to 2 K/km provided the average between this and higher levels within 2 km does not exceed 2 K/km" (World Meteorological Organization; WMO, 1957), while the CPT is the level of the minimum temperature.

The tropopause inversion layer (TIL) is a narrow layer about 1–2 km from the CPT that is characterized by a sharp change in the vertical gradient of the temperature profile, which is also recognized in the static stability profile (Grise et al., 2010; Bell and Geller, 2008; Birner, 2006; Birner et al., 2002). Using routine radiosonde sounding data, a strong mean inversion at the tropopause in the midlatitude was analyzed (Birner et al., 2002; Birner, 2006). Grise et al. (2010) conducted a global survey of the TIL characteristics, including annual cycle, horizontal distribution and interannual variations related to the stratospheric Quasi Biennial Oscillation (QBO) using the Global Positioning System Radio Occultation (GPS-RO) data. TIL is a boundary within the TTL that controls the mixing of air between the troposphere and stratosphere (e.g. Fujiwara and Takahashi, 2001). A very low temperature in the TTL causes dehydration of the air entering the stratosphere (Mote et al., 1996; Fueglistaler et al., 2009).

The static stability is expressed as the square of the Brunt Väisälä or buoyancy frequency (N^2). N^2 is the main factor in the dispersion relations for atmospheric waves, including medium-scale gravity waves and planetary-scale equatorial waves such as Kelvin waves and mixed Rossby–gravity waves (Andrews et al., 1987). Birner (2006) found that the mean N^2 shows enhanced values near the extratropical tropopause compared to the extratropical lower stratospheric values. Furthermore, Grise et al. (2010) found the largest magnitudes of N^2 between 10°−15° latitude in both hemisphere during northern hemisphere (NH) winter season. The spectrum of normalized temperature fluctuations associated with gravity waves is sensitive to change in N^2 (Smith et al., 1987; Fritts et al., 1988). Therefore, an accurate understanding of its horizontal distribution and temporal variations, particularly in the tropics, is important when investigating the characteristics of atmospheric wave propagation. The 20-day Kelvin wave propagation influences the structure of the tropopause height and the value of N^2 (Randel and Wu, 2005; Tsuda et al., 1994).

Randel and Wu (2005) demonstrated eastward phase tilt with height of Kelvin waves that modulate the climatological cold tropopause over Indonesia with the maximum amplitude near the tropical tropopause (~17 km). A long-term analysis using Singapore radiosonde data and GPS-RO results showed that Kelvin wave activity was stronger during the transition from the easterly to westerly phase of the QBO (Shiotani and Horinouchi, 1993; Randel et al., 2003; Ratnam et al., 2006). The El Niño and La Niña events, known as the El Niño Southern Oscillation (ENSO), considerably influence the equatorial wave activity and the TTL (Trenberth, 1997; Nishimoto and Shiotani, 2012; Scherllin-Pirscher et al., 2012). The intra-seasonal variation in the tropics, known as the Madden–Julian Oscillation (MJO), tends to be more active toward the Eastern Pacific during El Niño events (Son et al., 2017). The static stability in the upper troposphere tends to decrease with the deep convection associated with the MJO (Nishimoto and Yoden, 2017).

Holloway and Neelin (2007) found negative correlation of temperature perturbations between the free troposphere (about 800 – 200 hPa) and the convective cold top (about 100 – 50 hPa). The cooling in the convective cold top is due to a

hydrostatic adjustment to the deep convective heating (Holloway and Neelin, 2007). Paulik and Birner (2012) identified a typical temperature perturbations in the deep convective cloud associated with reduced ozone event, warm anomaly in the mid and upper troposphere and cold anomaly in the TTL. We are also interested in the characteristics of static stability in the TTL associated with the convective activity.

The sharp increase of N^2 across the tropopause (i.e., the sharpness) and the thickness of the layer of maximum N^2 above the tropopause (i.e., between 80% reaching to and decreasing from maximum N^2) have been determined in previous studies (Bell and Geller, 2008; Kim and Son, 2012) using both ground- and satellite-based observations (we describe this definition in Fig.2 left panel). For example, Bell and Geller (2008) analyzed the twice daily standard radiosonde data from WMO stations

10   and found that the thickness was ~1 km at low latitudes. Using data from the CHAllenging Mini satellite Payload (CHAMP) GPS-RO mission (Wickert et al., 2001), Schmidt et al. (2005) reported that the tropopause sharpness varies less throughout the year in the tropics than in polar regions. Ratnam et al. (2005), also using the CHAMP dataset, reported an association between greater sharpness and a higher and colder tropopause.

15   Since the launch of Constellation Observing System for Meteorology Ionosphere and Climate (COSMIC) GPS-RO in April 2006 (Anthes et al., 2008), which has a much greater number of occultations than CHAMP, investigation of the global characteristics of the tropical tropopause has intensified (e.g. Grise et al., 2010; Son et al., 2011; Kim and Son, 2012). The tropopause sharpness is defined as the difference between the mean N^2 ($\overline{N^2}$) in the region up to 1 km above the LRT or CPT ($\overline{N^2}_{+1}$), and $\overline{N^2}$ in the region down to 1 km below the LRT or CPT ($\overline{N^2}_{-1}$) (Kim and Son, 2012; Son et al., 2011). Son et al.

20   (2011) showed maximum sharpness over the Western Pacific region in all seasons with slightly higher values during NH winter, while Kim and Son (2012) reported that the local structure and seasonal variability of the tropopause sharpness are associated with convectively coupled equatorial waves. Averaging the N^2 profile within ±1 km of the LRT or CPT can reduce fluctuations caused by small-scale perturbations. Pilch Kedzierski et al. (2016) described the role of MJO, QBO, Kelvin, inertia–gravity, and Rossby waves in modulating the maximum N^2 ($maxN^2$) above the LRT in the tropics using the

25   long-term COSMIC dataset.

Fine-scale temperature profiles (T) from GPS-RO measurements commonly have ~1 km vertical resolution in the upper troposphere and lower stratosphere (UTLS) (Kursinski et al., 1997). The actual effective vertical resolution of RO measurements increases in region of increased refractive gradients such as inversion layers above the boundary layer or the

30   tropopause. Support from the COSMIC Data Analysis and Archive Center (CDAAC) allowed us to retrieve the dry temperature from COSMIC with higher resolution, reaching 0.1 km, in the UTLS (Noersomadi and Tsuda, 2017). We are motivated to utilize the long-term COSMIC GPS-RO data at a vertical resolution of 0.1 km to investigate the annual, interannual, and intra-seasonal variability in properties of the tropical tropopause; i.e., the static stability and TIL parameters (sharpness and thickness). We begin by describing the latitudinal and longitudinal distributions of N^2 with relative to CPT

35   height. After displaying N^2 distributions in the tropics, we investigate the relationships between TIL and ENSO variability, and between TIL and MJO activity.

2 Data

We briefly explain the difference between dry temperature from two COSMIC datasets, ***cosmicfsi*** and ***cosmic2013***, and their

40   comparison with radiosonde data. We use ***cosmic2013*** data only from October 2011 to March 2012 (183 days), the duration of the international collaborative campaign called the cooperative Indian Ocean experiment on intra-seasonal variability in

the year 2011 and the joint project of Dynamics of the Madden–Julian Oscillation (CINDY-DYNAMO 2011) (Yoneyama et al., 2013; Zhang et al., 2013). For the long-term analysis, we utilize *cosmicfsi* from 2007 to 2016 (10 years) to derive N^2 and determine the TIL parameters relative to the CPT. In the following, we outline details of high-resolution T profiles, TIL definitions, and supporting information.

2.1 High-resolution temperature profiles of COSMIC GPS-RO

The GPS limb soundings received by low Earth orbit satellites that pass through the lower stratosphere down to the troposphere may contain multipath atmospheric signals, such as atmospheric minor constituents and sharp gradients at the tropopause (Melbourne, 2004). COSMIC GPS-RO provides 1500–2000 profiles per day (~400 profiles over 10°S–10°N) (Anthes, 2011). Nevertheless, the number of profiles is significantly decreasing in 2015 and 2016 (60−100 profiles over 10°S–10°N). The COSMIC retrievals apply wave optics algorithms such as Full Spectrum Inversion (FSI) and Phase Matching (PM) (Jensen et al., 2003, 2004), transforming the entire phase and amplitude of the occultation signal to derive the dry atmospheric temperature profiles preserving vertical resolution of ~0.1 km at lower altitudes (Anthes, 2011; Gorbunov, 2002).

The *cosmicfsi* datasets use FSI up to 30 km altitude, but reliable T profiles representing small perturbations in the lower stratosphere due to atmospheric gravity waves are limited to below ~28 km due to increasing noise from the retrieval data processing (Tsuda et al., 2011). At altitudes above 30 km, T of *cosmicfsi* is obtained from the time derivative of the excess phase of the GPS signal (the geometrical optic method; Kursinski et al., 1997), which was used above 20 km for COSMIC data re-processed by CDAAC (*cosmic2013*). The *cosmic2013* dataset was retrieved using PM and smoothed over a 0.5 km scale in the range 10–20 km (Sokolovskiy et al., 2014; Zeng et al., 2016). There was good agreement between the T profiles in the UTLS for both COSMIC datasets and radiosonde data, and the mean difference of CPT temperatures was within ±0.4 K (Noersomadi and Tsuda, 2017). The discrepancy in the CPT altitude between *cosmicfsi* and the campaign radiosonde dataset was 70 m (mean) and 100 m (median) (Noersomadi and Tsuda, 2017). The *cosmicfsi* dataset is freely available on the Inter-university Upper atmosphere Global Observation NETwork (IUGONET) system of the metadata database of the Japanese inter-university research program (Hayashi et al., 2013).

We found 2,312 and 3,387 occultation profiles (~12 profiles/day and ~18 profiles/day) in *cosmicfsi* and *cosmic2013*, respectively, inside 90–150°E, 10°S–10°N (the Maritime Continent region) within a 183-day period in 2011/2012. The difference in the total number of occultations in the two retrievals is possibly caused by different algorithm and background extrapolation model for bending angles as reported by Noersomadi and Tsuda (2017). Discussion of difference between retrieval algorithm for *cosmicfsi* and for *cosmic2013* is beyond the scope of this study. To compare the shape of N^2 profiles derived from T by *cosmicfsi* and *cosmic2013* that have different vertical resolution, we use radiosonde observations collected during the CINDY-DYNAMO 2011 campaign. Table 1 lists the 13 stations in the Maritime Continent where approximately twice-daily routine balloon soundings with 2-s recording were conducted. The total number of radiosonde balloons lifted successfully up to >2 km above the CPT is 3,996 (~21 profiles/day). All radiosonde data were downloaded from the Earth Observing Laboratory (http://data.eol.ucar.edu).

We adjusted T from GPS-RO in the geometrical height domain to the geopotential height used for radiosonde data before performing the comparison. Figure 1 shows a typical COSMIC profile on 24 November 2011 at 12:43 UT, which is located within ~115 km horizontal radius from the balloon observation launched at 11:35 UT at Surabaya station (112.78°E, 7.37°S). Assuming the average ascent rate of the balloon is ~5 m s^{-1} (Gong and Geller, 2010), the temperature measurement at 18 km

occurred at around 12:35 UT, so the actual time difference with the occultation event is less than 30 min in the UTLS. The T from *cosmicfsi* agrees very well with the radiosonde result, particularly above 16.5 km. The *cosmicfsi* shows small-scale perturbations and large N^2 above the CPT, as shown in the radiosonde data.

5   The mean N^2 profiles of all available *cosmicfsi*, *cosmic2013*, and radiosondes within the 183-day period are shown in Fig. 2 (left). The N^2 profile just above the CPT from *cosmicfsi* that agreed very well with the radiosonde data is sharper than the N^2 from *cosmic2013*. Figure 2 (right) shows the zonal mean of N^2 over 10°S–10°N latitude throughout the 10 years of *cosmicfsi* data (329,396 profiles). The existence of a sharp thin layer is seen from the long-term *cosmicfsi* dataset. This study mainly discusses the sharpness (*S*-ab, where 'ab' means 'above' and 'below' the CPT) and thickness (*dH*), which are defined in Fig.
10   2 (right panel).

2.2 TIL definitions

There are several definitions of TIL related to N^2 behavior analyzed with GPS-RO data. Grise et al (2010) showed minor differences in the zonal mean N^2 profile relative to LRT and CPT in the tropics. Randel et al. (2007; 2010) and Wang et al.
15   (2013) investigate TIL using temperature gradient. Schmidt et al. (2005) and Son et al. (2011) defined the TIL with respect to LRT height; more recently, Gettelman and Wang (2015) and Pilch Kedzierski et al. (2016) used the definition with respect to LRT height. Ratnam et al. (2005) and Kim and Son (2012) defined the tropopause sharpness as the change in temperature gradient across the CPT. Considering that CPT is the appropriate reference for the tropical tropopause (Kim and Alexander, 2015), we define TIL parameters relative to CPT height in this study.

We obtain TIL parameters from the individual N^2 profiles, limiting the height range to ±3 km relative to the CPT, where most of the maximum and minimum peaks of N^2 are located. Definitions of the TIL parameters are summarized in Table 2. We define TIL sharpness as follows:

     1) *S*-aCPT is the difference between $maxN^2_{+1}$ and N^2 at the CPT,
25   2) *S*-bCPT represents the difference between N^2 at the CPT and minimum N^2_{-1} ($minN^2_{-1}$), and

     3) *S*-ab the difference between $maxN^2_{+1}$ and $minN^2_{-1}$ (i.e., *S*-ab is equal to the sum of *S*-aCPT and *S*-bCPT).

The TIL thickness definitions include:

     1) *dH*-aCPT and *dH*-bCPT are the corresponding distances of $maxN^2_{+1}$ and $minN^2_{-1}$ relative to the CPT, respectively,
30   2) *dH*-ab is the distance between height of $minN^2_{-1}$ and height of $maxN^2_{+1}$, and

     3) *dH* is the thickness over which $N^2 \geq 80\% maxN^2$

We will focus on seasonal variation of *S*-ab and *dH* in Section 3.3. We have analyzed how the results change quantitatively when using the difference between $maxN^2_{+1}$ and $minN^2_{-1}$ instead averaging along ±1 km relative to CPT as was done by Kim
35   and Son, (2012), with effectively higher vertical resolution dataset. In order to obtain *dH* we need to define the corresponding N^2 value. Considering the stable N^2 value in the lower stratosphere 6.5×10^{-4} s^{-2} and the $maxN^2$ 10.5×10^{-4} s^{-2} (Fig. 2 right panel), the threshold of N^2 should be larger than 65% of $maxN^2$. We choose 80% as the threshold.

The TIL parameters are sorted on a $5° \times 5°$ longitude and latitude grid. The grid cells with no available TIL data are denoted
40   as missing values. We analyze the frequency distribution and the climatology of TIL parameters in the region 0°–360°E, 30°S−30°N in the next section. To investigate the interannual and intra-seasonal variations, we focus on the low latitudes, 10°S−10°N. Due to the limited number of COSMIC profiles in each grid cell (1 or 2), we then averaged 5 days for data for

each grid cell recursively using simple arithmetic mean to determine the daily series data for investigating the TIL variations at intra-seasonal time-scales.

2.3 Additional data

To complement the analysis of TIL variations in the tropics, we use NOAA Outgoing Long Wave (OLR) data, which are considered a proxy for convective activity (Liebmann and Smith, 1996). We refer to the ENSO sea surface temperature (SST) Niño 3.4 index (accessed from http://www.cpc.ncep.noaa.gov/data/indices/ on 9 August 2018) to investigate the influence of El Niño and La Niña on convective activity and TIL variability at an interannual time-scale. When analyzing the intra-seasonal variations, we use the OLR MJO Index (OMI) (Kiladis et al., 2014; available at https://www.esrl.noaa.gov/psd/mjo/mjoindex/), which consists of the first two principal components (PC_1 and PC_2) of the empirical orthogonal functions of 30–96 day filtered OLR. OMI is considered as the index that represents the eastward propagation of deep convection (Kiladis et al., 2014; Nishimoto and Yoden, 2017). An MJO active phase is defined when the amplitude of OMI ($\sqrt{PC_1 + PC_2}$) ≥ 1; otherwise, MJO is inactive.

3 Results

3.1 Static stability in the tropics

We investigate the mean N^2 in the coordinate relative to CPT height by focusing on the 30°S–30°N latitude range over the Maritime Continent (MC; 90°–150°E) and the Pacific Ocean (PO; 170°–230°E). During DJF and JJA, both longitude regions have a single layer of ~0.5 km thick with large N^2 of ~12.0×10^{-4} s^{-2} (Fig. 3). The area of $N^2 \geq 10.0 \times 10^{-4}$ s^{-2} in DJF extends over 15°S–15°N over the MC, while it is limited to around 10°S–10°N over the PO. The area with $N^2 \geq 10.0 \times 10^{-4}$ s^{-2} in JJA is generally narrower than that in DJF. During DJF over the MC, values of N^2 of about $7.0–8.0 \times 10^{-4}$ s^{-2} are found over 10°–20°N and 10°–20°S between 1 and 2 km above the CPT. A similar pattern is seen over the PO but the enhancement of N^2 around 20°N and 20°S is smaller than that in the MC. We found the $maxN^2$ at range $11-12.0 \times 10^{-4}$ s^{-2} above CPT height in the two longitude regions. Note that Grise et al. (2010) reported that the zonal mean $maxN^2$ value above the LRT and CPT heights was ~8.0×10^{-4} s^{-2} using CHAMP dataset (see Fig. 2 in Grise et al, 2010). The different larger values found in this study are probably due to the use of data of higher effective vertical resolution.

The profiles of large N^2 over 20°N and 20°S in the MC region represent the vertical section of the Kelvin and mixed Rossby–gravity waves response known as the Matsuno–Gill pattern mode (Matsuno, 1966; Gill, 1980; Grise et al., 2010; Nishimoto and Shiotani, 2012). The results shown in Fig. 3 uncover the detail structure of N^2 above CPT in the specific longitude regions compared to the results by Grise et al. (2010) that showed the mean N^2 over $0-1$ km layer above LRT. The vertical propagation of equatorial waves (Kelvin waves and/or gravity waves), as the results of convective forcing, modulates the tropopause (Tsuda et al., 1994; Randel and Wu, 2005; Kim and Alexander, 2015; Kim et al., 2018). The MJO activity was also found to control the tropopause variability (Kim and Son, 2012; Pilch Kedzierski et al., 2016).

The N^2 above the tropical tropopause in DJF is larger than in JJA in the longitude–height cross-section over 10°S–10°N (not shown). The mean N^2 has a maximum of about 8×10^{-4} s^{-2} at 17.5−19.0 km which agrees with the result by Grise et al (2010). This height range is located around 1–2 km above the mean LRT height (16.5 km). The $maxN^2$ of individual profiles are located mainly within 1 km above the CPT height (17.2 km). Averaging N^2 in conventional height coordinates tends to smooth out the tropopause sharpness (Birner et al., 2002). Here, we describe the longitude–height cross-section of N^2

distribution relative to the CPT height (Fig. 4). The region of elevated N^2 becomes a single thin layer with maximum value reaching 12.0×10^{-4} s^{-2}. Values of $N^2 \geq 10.0 \times 10^{-4}$ s^{-2} are more prominent in DJF than in JJA (Fig. 3). Values of $N^2 \geq 7.0 \times 10^{-4}$ s^{-2} at 1–2 km above CPT are shifted somewhat eastward from the maximum at 0.0–0.5 km above the CPT, especially at 120°–210°E and 240°–300°E.

Figures 3 and 4 show a thin layer of low N^2 within the 1 km layer below the CPT and large N^2 within the 1 km above the CPT. In the following section we investigate the frequency distribution of TIL parameters related to the shallow layer within ±1 km of the CPT.

10 **3.2 Frequency distribution of TIL parameters**

The histograms of all TIL parameters over the period 2007–2016 for the entire longitude range at 30°S–30°N are presented in Fig. 5. All parameters show a skewed distribution. In Fig. 5 (left column), the mean S-aCPT is larger than S-bCPT. The values of S-aCPT are mostly in the range 2.8–6.6×10^{-4} s^{-2}, and the values larger than its mean in the range 8.4–18.0×10^{-4} s^{-2}. About 80% of S-bCPT values lie in the range 1.7–6.2×10^{-4} s^{-2}, while only about 3% have S-bCPT $> 8.0 \times 10^{-4}$ s^{-2}. The

15 mean and standard deviation of S-ab are $(10.5 \pm 3.7) \times 10^{-4}$ s^{-2}. The tail to the right of the mean S-ab is longer than that to the left (i.e., positive skewness). The positive skewness distribution of S-ab is found to be similar to the results by Pilch Kedzierski et al. (2016) for $maxN^2_{+1}$ above LRT for both easterly and westerly QBO periods. This is reasonable since $maxN^2_{+1}$ above CPT would dominate the relatively low values of $minN^2_{-1}$ below CPT, showing similar features to those of S-ab. The results indicate a large variation in temperature gradient within 1 km above the CPT. The natural question would be

20 when and where large values (the longer tails) appear and what atmospheric processes are responsible. In the next section, we discuss the variation in S-ab that is associated with convective activity.

The distribution of dH-aCPT, which has mean and standard deviation 0.4 ± 0.2 km, is similar to that of S-aCPT, while dH-bCPT is nearly symmetric with mean and standard deviation 0.5 ± 0.2 km (Fig. 5 right column). About 60% of the values of

25 dH-aCPT lie in the range 0.2–0.4 km. That means that 60% of $maxN^2$ are located between the CPT and 0.4 km above it. About 70% of the magnitudes of dH-ab are within 1.0 ± 0.2 km. This is reasonable because dH-ab is equal to the sum of dH-aCPT and dH-bCPT, and this means the distance between the $minN^2$ level below the CPT and the $maxN^2$ level above CPT was 1 km. The $minN^2$ and $maxN^2$ are related to decreasing and increasing temperature, respectively.

30 The thickness dH varies between 0.3 and 0.6 km, but 70% of the values are within 0.4 ± 0.04 km (green histogram in Fig. 5, lower right panel). This result shows a very thin TIL layer above the CPT in the tropics. The thin layer of TIL can also be seen in Fig. 3. If the mean $maxN^2$ is in the range 11–12×10^{-4} s^{-2} in both seasons, then 80% of the $maxN^2$ is about 8.8–9.6 $\times 10^{-4}$ s^{-2}. The contour lines of N^2 at this interval depict a very thin layer (<0.5 km) in both longitude regions (Fig. 6). This leads to the question of how the thickness varies in the tropics. In the following section, we investigate the climatology

35 of dH.

3.3 Seasonal variations in TIL sharpness and thickness

Figure 6 shows horizontal distributions of the mean S-ab, dH, and OLR in the tropics during DJF and JJA. The mean S-ab in the low latitudes during DJF is larger than that during JJA. The highest values, up to 16–18×10^{-4} s^{-2}, are considerably

40 associated with low OLR values, suggesting strong deep convection over the following convective regions: (i) Africa, (ii) a wide area from the Maritime Continent to the Western Pacific, and (iii) South America. Large S-ab values are found along in

the equator region, while low OLR regions show latitudinal variation with season. Local and seasonal variability of horizontal structure of tropopause sharpness presented in this work are consistent with previous studies which attributed it to equatorial waves activity (e.g. Grise et al., 2010; Son et al., 2011; Kim and Son, 2012). However, we found different quantitative result in particular over the Western Pacific because of the use of $maxN^2_{+1}$ and $minN^2_{-1}$ instead of averaging N^2

5   within ±1 km relative to CPT by Kim and Son (2012). Maximum static stability just above the tropical tropopause could also be associated with divergence flow as demonstrated by Pilch Kedzierski et al., (2016). Large S–ab around the 240°–270°E longitude region in DJF is qualitatively related to OLR values of 220–240 W m^{-2} representing the inter tropical convergence zone (ITCZ). Large S-ab values of 14–16×10^{-4} s^{-2} are also found over South Asia and near the ITCZ in JJA. Exception is seen over South America where S-ab only reaches $\sim14 \times 10^{-4}$ s^{-2} associated with OLR values < 220 W m^{-2}. Radiative effects

10   from cirrus cloud may be responsible for the enhancement of S-ab. Sassen et al. (2009) demonstrated that cirrus clouds are confined to the monsoon region and ITCZ where they are generated in anvils created by deep convection. The cirrus cloud decreases the static stability below the tropopause (Nishimoto and Yoden, 2017; Son et al., 2017). Therefore, decreasing static stability below the tropopause will tend to enlarge the difference between $maxN^2_{+1}$ and $minN^2_{-1}$.

15   Bell and Geller (2008) investigated the thickness defined as the distance from the LRT to the level where dN^2/dz reached its minimum in the stratosphere (z is the vertical coordinate) using global interpolated radiosonde data. They reported a thickness of ~1 km at latitudes around 15°N. Since there are few radiosonde stations in the low latitudes, they did not show the horizontal distribution of the thickness. Here, we use a different definition of dH as explained in Section 2. In Fig. 6 (middle row), values of dH lie in the range 0.39–0.48 km. Large dH associated with low OLR values over the three

20   convective regions agrees qualitatively with large S-ab.

Deep convection over Indonesia and northern Australia near Darwin during the Australian monsoon (DJF) and over the Bay of Bengal, South Asia, and the Philippines during the Asian monsoon (JJA) seems to be the main control on S-ab and dH. To emphasize the effect of convective activity, we show the mean N^2 profiles in DJF and JJA in Fig. 7. We define 90°–140°E,

25   10°S–0 in DJF and 80°–130°E, 10°N–20°N in JJA as the "convective" regions (OLR ≤ 240 W m^{-2}). The "non-convective" regions (OLR > 240 W m^{-2}) are 200°–250°E, 10°S–0 in DJF and 190°–240°E, 15°N–25°N in JJA. We selected those regions as described in Fig. 6 (bottom row), each with the same area (50° longitude × 10° latitude). The total numbers of profiles from 10 years of COSMIC GPS-RO observation inside the convective regions are 9,140 in DJF and 18,046 in JJA, while inside the non-convective regions there are 8,758 profiles in DJF and 17,103 in JJA. COSMIC satellites operate in polar

30   orbits, so the highest numbers of profiles are located in mid-latitudes (e.g., Fig. 1 in Son et al., 2011). The total numbers of profiles in JJA are larger than in DJF because the convective and non-convective regions in JJA are defined to lie closer to the mid-latitudes. It is clear that in both DJF and JJA the mean N^2 over the convective regions is smaller below the CPT and larger above CPT than the mean N^2 over the non-convective regions. The difference of the mean N^2 is $\sim0.5 \times 10^{-4}$ s^{-2} below the CPT and $\sim1.3 \times 10^{-4}$ s^{-2} near the level of $maxN^2$ above the CPT. The observations show that regions with more frequent

35   convective activity show decreased N^2 below CPT and increased $maxN^2_{+1}$, which increased S-ab from 9.4×10^{-4} s^{-2} to 10.4×10^{-4} s^{-2} and tended to increase dH from 0.3 to 0.5 km.

We have examined the spatial distributions of S-ab and dH in boreal winter and summer. To show the seasonal cycle in the different longitude regions, we calculated the monthly mean and standard deviation of S-ab and dH over 10°S–10°N as

40   shown in Fig. 8. We repeat two seasonal cycles in Fig. 8 to display seasonal cycle more clearly. The sharpness and thickness are greater in MC than in PO. The sharpness in MC during July–August is somewhat higher than in May–June and September–October, while it is relatively constant at 11×10^{-4} s^{-2} in PO from March to November. It is also clear that the

seasonal cycle in MC is affected by sub-seasonal variation. On the other hand, the thickness in PO shows a clear annual cycle with a minimum in JJA. The results indicate that land–sea distribution influences the variability in S-ab and dH.

In the following section we discuss the interannual and intra-seasonal variability of S-ab.

3.4 Influence of El Niño and La Niña

We investigate the monthly mean S-ab as well as OLR data in the two longitude regions (Fig. 9). Large S-ab in the MC associated with low OLR values can be seen during NH winter as part of the annual cycle. Neither the annual peak of S-ab nor the peak of low OLR over the MC is seen in DJF for 2009–2010. On the other hand, S-ab increased from $\sim 11 \times 10^{-4}$ s^{-2}

10 to 12×10^{-4} s^{-2} over the PO in the same period. This suggests a signal of interannual variation in S-ab and OLR in both the MC and PO. Another signal that can be interpreted as interannual variation is seen in DJF of 2015–2016, where S-ab showed a strong peak and convective activity was also enhanced in the PO. The linear correlation between S-ab and OLR in the MC and PO has coefficients of −0.57 and −0.67, respectively, delineating an out-of-phase relation. We have tested for different lags. The cross-correlation between S-ab and OLR become smaller for two month lag (−0.49 and −0.57 over MC and PO

15 regions, respectively).

The negative correlation from the monthly mean time series may still be affected by the annual cycle or intra-seasonal variation. Therefore, we investigate the S-ab and OLR anomalies (S-ab* and OLR*) calculated by subtracting the climatological values from the monthly mean time series. Next, we compare both S-ab* and OLR* with the SST Nino 3.4

20 index (Fig. 10). We applied a 4-month running mean to smooth the time series and reduce the possible intra-seasonal fluctuation, as subtracting the climatological mean will only remove the annual cycle. El Niño events were defined when SST Niño 3.4 > +0.5. Strong El Niño events occurred during the NH winters 2009–2010 and 2015–2016. La Niña events were determined when SST Niño 3.4 < −0.5. La Niña events were seen during the NH winters 2007–2008, 2008–2009 and 2010–2011. A linear correlation analysis shows that S-ab* is negatively correlated with both OLR* (−0.56) and SST Niño

25 3.4 (−0.66) in the MC. Surprisingly, in the PO, S-ab* is strongly negatively correlated with OLR* (−0.90) and strongly positively correlated with SST Niño 3.4 (+0.88). The negative and positive correlations between S-ab* and SST Nino3.4 show that El Niño and La Niña phenomena have a significant impact on the variation in S-ab*. The high magnitude of the correlation for PO could be due to the fact that, outside ENSO events, this is a region with very low convective activity, whereas MC is not devoid of convection even during ENSO events (and MJO can influence the MC region as well in its late

30 phases). The negative correlation between S-ab* and OLR*, which is modulated by SST Niño 3.4, means that convective activity on the interannual time-scale influences S-ab* in both longitude regions.

To analyze in more detail the influence of El Niño and La Niña, we calculate the mean N^2 profile over the MC and PO during DJF El Niño and DJF La Niña (Fig. 11). The mean N^2 during La Niña events below the CPT was smaller and above

35 the CPT was larger than during El Niño events over the MC, as more convection occurred. Under La Niña conditions, the mean $maxN^2$ overshoots up to 12×10^{-4} s^{-2} and relaxes gradually to the lowermost stratospheric value of 6×10^{-4} s^{-2} at 2 km above the CPT. However, under El Niño conditions the mean $maxN^2$ is $\sim 10 \times 10^{-4}$ s^{-2} and sharply decreases to 6×10^{-4} s^{-2} about 0.5 km above the CPT. Convective clouds that are more active during El Niño in the PO than during La Niña are the cause of the difference in mean N^2 profiles between these two cases shown in Fig. 11 (middle). The $maxN^2$ in El Niño was

40 11.4×10^{-4} s^{-2}, larger than in La Niña (10×10^{-4} s^{-2}), but in both cases the values of N^2 sharply decrease then coincide at the lowermost stratospheric value at ~ 1 km above the CPT. The results show that convective activity in both longitude regions

during El Niño and La Niña will extend the $maxN^2_{+1}$ above the CPT so that S-ab increases from 9.4×10^{-4} s^{-2} to 10.9×10^{-4} s^{-2}.

Figure 11 (right) shows the difference in the mean N^2 (ΔN^2) between El Niño and La Niña events. In the MC and PO, the ΔN^2 below the CPT is ~0.5×10^{-4} s^{-2} in both cases. We found that above the CPT the peak amplitude ΔN^2 in the MC regions is higher and larger (0.5 km above the CPT and 1.8×10^{-4} s^{-2}) than in the PO region (0.2 km above CPT and 1.4×10^{-4} s^{-2}). The difference in the thermal structure near tropopause over land and ocean may cause the difference in peak amplitude of ΔN^2 above the CPT. One possibility is that is that the mountainous characteristics of the MC region are favorable to generate convectively couple equatorial waves (Kubokawa et al., 2016). Other possible processes are as follows. Warmer SST under La Nina conditions results in more active convection that tends to force air upward to the TTL and then decrease the static stability below the CPT. The stratospheric air resists a change in height, so the temperature gradient becomes greater, enhancing $maxN^2$ above the CPT. Although our analysis is based on limited observations, the results indicate that tropopause sharpness is correlated with convective activity associated with El-Niño and La-Niña phenomena.

3.5 MJO modulation

The convective activity in the tropics is also influenced by intra-seasonal variability (Wheeler and Kiladis, 1999). We extend our analysis to the intra-seasonal variation in tropopause sharpness related to MJO propagation in the tropics. An MJO active phase is represented by large-scale deep convection that moves eastward, while an inactive phase is marked by suppressed convection (Zhang, 2005). Organized convective clouds propagate from the Indian Ocean to the Western Pacific from phase 3 to phase 6, as defined by Wheeler and Hendon (2004), over a period of ≤10 days or within 10−15 days during fast MJO episodes. During slow MJO episodes the propagation takes more than 20 days (Yadav and Straus, 2017). To identify fast or slow MJO events, we use OMI data because they are derived directly from OLR and represent the convective signal of MJO (Kiladis et al., 2014). Figure 12 shows case study for a slow MJO episode from 1 December 2007 to 28 February 2008 and a fast MJO episode from 15 January 2012 to 15 April 2012. The figure shows the propagation for both MJO active and inactive phases. In this figure, we obtained S-ab* by subtracting the average of S-ab over 120 days from the 5-day running mean time series. We applied a band-pass filter to the fluctuation components of S-ab with a cut-off frequency of 30–90 days to retain MJO phase propagation (Kiladis et al., 2014; Zhang, 2005). The same analysis was applied to the OLR data.

Enhancement of S-ab* is obviously associated with eastward propagation of organized deep convection from the western Indian Ocean to the central Pacific during December 2007 and January 2008 (~60 days), which is classified as a slow MJO episode (Fig. 12 left). During the fast MJO episode (Fig. 12 right), eastward movement of large positive S-ab* also coincided with negative OLR* from January 23 to February 8, 2012 (a period of 17 days). When the deep convection was suppressed during the inactive phase, S-ab* decreased. Zeng et al. (2012) demonstrated cold temperature anomaly observed with COSMIC near the tropopause associated with rainfall anomaly during MJO active phase propagation. Kim and Son (2012) and Pilch Kedzierski et al. (2016) also found MJO signal modulates the tropopause temperature and sharpness structure using COSMIC temperature data. We found that the MJO propagation in the tropics has an impact on the variability in tropopause sharpness, being consistent with the results by Pilch Kedzierski et al. (2016). Note that, we demonstrated time evolution of positive sharpness anomaly associated with negative OLR anomaly, which is not shown in the previous studies (Kim and Son, 2012; Pilch Kedzierski et al., 2016). A strong correlation between S-ab* and OLR* propagation on the intra-seasonal time-scale indicates that the organized deep convection reaches the upper troposphere and tends to enhance the temperature gradient in the TTL.

We investigated the N^2 profiles over the MC during the MJO active (5–15 January 2008) and MJO inactive (15–25 February 2008) phases. Figure 13 shows the characteristics of the difference in the mean N^2 between the periods of strong and weakened convection over the MC. The difference in the mean N^2 (ΔN^2) between the MJO active and inactive phases shows negative values of ~1×10^{-4} s^{-2} at 1–3 km below the CPT, then jumps to 5×10^{-4} s^{-2} within 0.5 km above the CPT, suggesting that convection tends to lower the static stability below the CPT and increase the static stability just above it. It is well known that vertical structure of temperature perturbations associated with deep convection indicate warm anomaly in the middle and upper troposphere and cold anomaly near the tropopause (e.g. Holloway and Neelin, 2007; Paulik and Birner, 2012). Adiabatic cooling near the tropopause is a natural response of the diabatic warming due to convection as a result of hydrostatic adjustment (Holloway and Neelin, 2007). Kim et al (2018) hypothesized that cold anomaly near the tropopause associated with organized deep convection during the MJO active phase is due to dehydration processes. This explains the large values of S-ab of 13.9×10^{-4} s^{-2} that form part of the long tail in the frequency distribution (Fig. 5).

To show the relationship between the convective activity and tropopause sharpness in MC and PO regions at intra-seasonal (Fig. 12) through to interannual time scales (Fig. 10), we provide the diagrams in Fig. 14 which are analogous to the Fig. 3 of Pilch Kedzierski et al. (2016) that showed sharpness versus divergence near the tropopause, and to Fig. 5 of Randel et al. (2007) that demonstrated sharpness versus vorticity in the extratropics. Figure 14 displays the scatter plot of S-ab versus OLR in all seasons. As expected, large S-ab values at range $9-18 \times 10^{-4}$ s^{-2} associated with OLR values of $250-150$ W m^{-2} for the number of sample > 180. We have also investigated the slope of relationship between S-ab and OLR in the top panel of Fig. 14 for the number of samples ≥ 500. Both slopes show only slightly difference between MC and PO regions, indicating that the variability of deep convection is the major cause of tropopause sharpness variability.

4 Concluding remarks

COSMIC GPS-RO data retrieved using Full Spectrum Inversion (***cosmicfsi***) provide 0.1 km vertical resolution temperature profiles (T) in the UTLS. Using these data for 2007 to 2016, we investigated the distribution of N^2 in the TTL and the variation in the tropical TIL. We showed that ***cosmicfsi*** captured small scale fluctuation in the individual N^2 as seen in radiosonde observation (Fig. 1). We demonstrated the characteristics of N^2 over the MC and PO relative to the CPT height. The maximum of the mean N^2 changed is ~12.0×10^{-4} s^{-2} within 1 km above the CPT. Latitudinal and longitudinal distributions show that N^2 above the CPT in DJF was larger than in JJA (Fig. 3 and 4). The results generally agree very well with previous studies (Grise et al., 2010; Birner, 2006; Birner et al., 2002). Using dataset with improved vertical resolution, we found larger values of N^2 compared to the results by Grise et al (2010) in this study.

We found that ~60% of $maxN^2$ values were located within 0.5 km above the CPT. The frequency distribution of the tropopause sharpness (S-ab) has a positive skewness with a longer tail to the right of the mean than to the left. The mean and standard deviation of S-ab are $(10.5 \pm 3.7) \times 10^{-4}$ s^{-2} (Fig. 5). This suggests a large variation in the temperature gradient within ± 1 km of the CPT. Typical TIL thickness (dH) values are in the range within 0.5 km. Analysis of the seasonal variation shows that large S-ab and large dH are associated with deep convection during the Australian and Asian monsoons (Fig. 6). In convective regions the mean N^2 is smaller below the CPT and larger above the CPT than in non-convective regions.

We analyzed the interannual variation in S-ab (S-ab*) and OLR (OLR*) anomalies, and the SST Nino 3.4 index. We found an out-of-phase relation between S-ab* and OLR* over both the Maritime Continent (MC) and Pacific Ocean (PO), with correlation coefficients -0.56 and -0.90, respectively. S-ab* in the MC was negatively correlated with SST Niño 3.4

(−0.66), while in the PO it was in-phase and strongly correlated (+0.88) (Fig. 10). We also calculated the mean N^2 over the MC and PO during DJF El Niño and DJF La Niña. The results indicate that during La Niña over the MC and El Niño over the PO, warmer SST gives more convection that tends to drive air upward in the TTL and increases the temperature gradient (positive S-ab*).

We also analyzed the intra-seasonal variation in S-ab*. Case studies during slow and fast MJO episodes show strong eastward propagation of S-ab* associated with deep convection. Meanwhile, when organized deep convection is suppressed in the MJO inactive phase, S-ab* decreases (Fig. 12). This suggests that the variations in S-ab* in the tropics are strongly related to the convective activity at this time-scale. We showed influence of ENSO and MJO on the variation of TIL that has not been studied previously. The diagram of S-ab versus OLR both in the MC and PO regions during all seasons indicates that the variability of convective activity in the tropics is the major cause of tropopause structure at various time scales (Fig. 14).

Acknowledgements

This work is supported in part by the Japan Society for the Promotion of Science (JSPS KAKENHI) Grant Number JP18K03741. Fruitful discussion with Prof. Shigeo Yoden is acknowledged. Author (N) received scholarship from Research and Innovation in Science and Technology Project (Riset-Pro), Ministry of Research, Technology and Higher Education (Kemenristekdikti) of Indonesia. The ***cosmicfsi*** data are freely available in the website (http://database.rish.kyoto-u.ac.jp/arch/iugonet/GPS/index.html) that is connected to the IUGONET database system (www.search.iugonet.org).

References

Andrews, D. G., Holton, J. R., and Leovy, C. B.: Middle atmosphere dynamics, International Geophysics Series, Vol. 40, Academic Press, 1987.

Anthes, R. A., Ector, D., Hunt, D. C., Kuo, Y. H., Rocken, C., Schreiner, W. S., … Yen, N. L. : The COSMIC/FORMOSAT-3 mission: Early results. Bulletin of the American Meteorological Society, 89(3), 313–333. https://doi.org/10.1175/BAMS-89-3-313, 2008.

Anthes, R. A.: Exploring Earth's atmosphere with radio occultation: Contributions to weather, climate and space weather, Atmos. Meas. Tech., 4, 1077–1103, doi:10.5194/amt-4-1077-2011, 2011.

Bell, S. W., and Geller, M. A.: Tropopause inversion layer: Seasonal and latitudinal variations and representation in standard radiosonde data and global models, J. Geophys. Res. -Atmos., 113, 1–7, doi:10.1029/2007JD009022, 2008.

Birner, T., Dörnbrack, A., and Schumann, U.: How sharp is the tropopause at midlatitudes?, Geophys. Res. Lett., 29, 1700, doi:10.1029/2002GL015142, 2002.

Birner, T.: Fine-scale structure of the extratropical tropopause region, J. Geophys. Res., 111, D04104, doi:10.1029/2005JD006301, 2006.

Butchart, N.: The Brewer-Dobson circulation, Rev. Geophys, 52, 157–184, doi:10.1002/2013RG000448, 2014.

Fritts, D. C., Tsuda, T., Sato, T., Fukao, S., and Kato, S.: Obervational evidence of a saturated gravity wave spectrum in the troposphere and lower stratosphere, J. Atmos. Sci., 45, 1741–1759, 1988.

Fueglistaler, S., Dessler, A. E., Dunkerton, T. J., Folkins, I., Fu, Q., and Mote, P. W.: Tropical tropopause layer, Rev. Geophys. 47, RG1004, doi(2008), 101029/, doi:10.1029/2008RG000267, 2009.

Fujiwara, M., and Takahashi, M.: Role of the equatorial Kelvin wave in stratosphere-troposphere exchange in a general

circulation model, J. Geophys. Res. -Atmos., 106, 22763–22780, doi:10.1029/2000JD000161, 2001.

Gettelman, A., and Wang, T.: Structural diagnostics of the tropopause inversion layer and its evolution, J. Geophys. Res., 120, 46–62, doi:10.1002/2014JD021846, 2015.

Gill, A. E.: Some simple solutions for heat-induced tropical circulation, Q. J. Roy. Meteorol. Soc., 106, 447–462, 1980.

5   Gong, J., and Geller, M. A.: Vertical fluctuation energy in United States high vertical resolution radiosonde data as an indicator of convective gravity wave sources, J. Geophys. Res., 115, D11110, doi:10.1029/2009JD012265, 2010.

Gorbunov, M. E.: Radio-holographic analysis of Microlab-1 radio occultation data in the lower troposphere, J. Geophys. Res., 107, 4156, doi:10.1029/2001JD000889, 2002.

10   Grise, K. M., Thompson, D. W. J., and Birner, T.: A global survey of static stability in the stratosphere and upper troposphere, J. Clim., 23, 2275–2292, doi:10.1175/2009JCLI3369.1, 2010.

Hayashi, H., Koyama, Y., Hori, T., Tanaka, Y., Abe, S., Shinbori, A., Kagitani, M., Kouno, T., Yoshida, D., Ueno, S., Kaneda, N., Yoneda, M., Umemura, M., Tadokoro, H., Motoba, T.: Inter-University upper Atmosphere Global Observation Network (IUGONET). Data Science Journal. 12, WDS179–WDS184, doi:10.2481/dsj.WDS-030, 2013.

15   Holton, J. R., Haynes, P. H., Mcintyre, M. E., Douglass, A. R., Rood, R. B. and Pfister, L.: Stratosphere-Troposphere Exchange, Rev. Geophys., 403–439, 1995.

Holloway, C. E., & Neelin, J. D.: The convective cold top and quasi equilibrium. Journal of the Atmospheric Sciences, 64(5),1467–1487, https://doi.org/10.1175/JAS3907.1, 2007.

Jensen, A. S., Lohmann, M. S., Benzon, H. H. and Nielsen, A. S.: Full spectrum inversion of radio occultation signals, Radio
20   Sci., 38, 1–15, doi:10.1029/2002RS002763, 2003.

Jensen, A. S., Lohmann, M. S., Nielsen, A. S. and Benzon, H. H.: Geometrical optics phase matching of radio occultation signals, Radio Sci., 39, 1–8, doi:10.1029/2003RS002899, 2004.

Kedzierski, R. P., Matthes, K. and Bumke, K.: The tropical tropopause inversion layer: Variability and modulation by equatorial waves, Atmos. Chem. Phys., 16, 11617–11633, doi:10.5194/acp-16-11617-2016, 2016.

25   Kiladis, G. N., Dias, J., Straub, K. H., Wheeler, M. C., Tulich, S. N., Kikuchi, K., Weickmann, K. M. and Ventrice, M. J.: A Comparison of OLR and Circulation-Based Indices for Tracking the MJO, Mon. Weather Rev., 142, 1697–1715, doi:10.1175/MWR-D-13-00301.1, 2014.

Kim, J. and Son, S. -W.: Tropical cold-point tropopause: Climatology, seasonal cycle, and intraseasonal variability derived from COSMIC GPS radio occultation measurements, J. Clim., 25, 5343–5360, doi:10.1175/JCLI-D-11-00554.1,
30   2012.

Kim, J.-E., and Alexander, M. J.: Direct impacts of waves on tropical cold point tropopause temperature, Geophys. Res. Lett., 42, 1584–1592, doi:10.1002/2014GL062737, 2015.

Kim, J., Randel, W. J., & Birner, T.: Convectively driven tropopause-level cooling and its influences on stratospheric moisture. Journal of Geophysical Research: Atmospheres, 123, 590–606. https://doi.org/10.1002/2017JD027080,
35   2018.

Kubokawa, H., M. Satoh, J. Suzuki, and M. Fujiwara: Influence of topography on temperature variations in the tropical tropopause layer, J. Geophys. Res. Atmos., 121, 11,556–11,574, doi:10.1002/2016JD025569, 2016.

Kursinski, E. R., Hajj, G. A., Schofield, J. T., Linfield, R. P. and Hardy, K. R.: Observing Earth's atmosphere with radio occultation measurements using the Global Positioning System, J. Geophys. Res., 102(D19), 23,429-23,465,
40   doi:10.1029/97JD01569, 1997.

Liebmann, B., Smith, C. A.: Description of a complete (interpolated) outgoing longwave radiation dataset, 1275–1277, 1996.

Matsuno, T. : Quasi-geostrophic motions in the equatorial area, J. Meteorol. Soc. Jpn., 44, 25–42, 1966.

Melbourne, W. G.: Radio occultation using earth satellites, Wiley., 2004.

Mote, P. W., Rosenlof, K. H., Mclntyre, M. E., Carr, E. S., Gille, J. C., Holton, J. R., Kinnersley, S., Pumphrey, H. C., Russel III, J. M., and Waters, J. W.: The imprint of tropical tropopause temperatures on stratospheric water vapor, J. Geophys. Res, 101, 3989–4006, 1996.

Nishimoto, E., and Shiotani, M.: Seasonal and interannual variability in the temperature structure around the tropical tropopause and its relationship with convective activities, J. Geophys. Res., 117, 1–11, doi:10.1029/2011JD016936, 2012.

Nishimoto, E., and Yoden, S.: Influence of the stratospheric quasi-biennial oscillation on the Madden–Julian oscillation during Austral summer, J. Atmos. Sci., 74(4), 1105–1125, doi:10.1175/JAS-D-16-0205.1, 2017.

Noersomadi and Tsuda, T.: Comparison of three retrievals of COSMIC GPS radio occultation results in the tropical upper troposphere and lower stratosphere, Earth Planets Space., 69, doi:10.1186/s40623-017-0710-7, 2017.

Paulik, L. C., & Birner, T.: Quantifying the deep convective temperature signal within the tropical tropopause layer (TTL). Atmospheric Chemistry and Physics, 12(24), 12,183–12,195. https://doi.org/10.5194/acp-12-12183-2012, 2012.

Randel, W. J., Wu., F., Rios, W. R.: Thermal variability of the tropical tropopause region derived from GPS/MET observations, J. Geophys. Res., 108, 4024, doi:10.1029/2002JD002595, 2003.

Randel, W. J., & Wu, F.: Kelvin wave variability near the equatorial tropopause observed in GPS radio occultation measurements, Journal of Geophysical Research, 110, D03102. https://doi.org/10.1029/2004JD005006, 2005.

Randel, W. J., Wu, F., and Forster, P.: The extratropical tropopause inversion layer: Global observations with GPS Data, and a radiative forcing mechanism, J. Atmos. Sci., 64, 4489–4496, doi:10.1175/2007JAS2412.1, 2007.

Randel, W. J., and F. Wu: The polar summer tropopause inversion layer, J. Atmos. Sci., 67, 2572–2581, doi:10.1175/ 2010JAS3430.1, 2010.

Ratnam, M. V., Tsuda, T., Shiotani, M., and Fujiwara, M.: New characteristics of the tropical tropopause revealed by CHAMP / GPS Measurements, SOLA, doi:10.2151/sola.2005, 2005.

Ratnam, M. V., Tsuda, T., Kozu, T., and Mori, S.: Long-term behavior of the Kelvin waves revealed by CHAMP / GPS RO measurements and their effects on the tropopause structure, Ann. Geophys., 1355–1366, doi:10.5194/angeo-24-1355-2006, 2006.

Sassen, K., Wang, Z., and Liu, D.: Global distribution of cirrus clouds from CloudSat/cloud-aerosol lidar and infrared pathfinder satellite observations (CALIPSO) measurements, J. Geophys. Res. -Atmos., 114, 1–12, doi:10.1029/2008JD009972, 2009.

Scherllin-Pirscher, B., Deser, C., Ho, S. -P., Chou, C., Randel, W., and Kuo, Y. -H.: The vertical and spatial structure of ENSO in the upper troposphere and lower stratosphere from GPS radio occultation measurements, Geophys. Res. Lett., 39, 2–7, doi:10.1029/2012GL053071, 2012.

Schmidt, T., Heise, S., Wickert, J., Beyerle, G., and Reigber, C.: GPS radio occultation with CHAMP and SAC-C : global monitoring of thermal tropopause parameters, Atmos. Chem. Phys., 1473–1488, doi:10.5194/acp-5-1473-2005, 2005.

Schmidt, T., Cammas, J. P., Smit, H. G. J., Heise, S., Wickert, J., and Haser, A.: Observational characteristics of the tropopause inversion layer derived from CHAMP/GRACE radio occultations and MOZAIC aircraft data, J. Geophys. Res. Atmos., 115(24), 1–16, doi:10.1029/2010JD014284, 2010.

Shiotani, M., and Horinouchi, T.: Kelvin wave activity and the quasi-biennial oscillation in the equatorial lower stratosphere, J. Meteorol. Soc. Japan, 75, 175–182, 1993.

Smith, S. A., Fritts, D. C., VandZandt, T. E.: Evidence for a saturated spectrum of atmospheric gravity waves, J. Atmos. Sci., 44(10), 1404–1410, 1987.

Sokolovskiy, S., Schreiner, W., Zeng, Z., Hunt, D., Kuo, Y. -H, Meehan, T. K., Stecheson, T.W., Manucci, A.J., Ao, C.O.: Use of the L2C signal for inversions of GPS radio occultation data in the neutral atmosphere, GPS Solut, 18, 404−416, doi:10.1007/s10291-013-0340-x, 2014.

Son, S. -W., Tandon, N. F., and Polvani, L. M.: The fine-scale structure of the global tropopause derived from COSMIC GPS radio occultation measurements, J. Geophys. Res. Atmos., 116, 1–17, doi:10.1029/2011JD016030, 2011.

Son, S. -W., Lim, Y., Yoo, C., Hendon, H. H., and Kim, J.: Stratospheric control of the madden-julian oscillation, J. Clim., 30, 1909–1922, doi:10.1175/JCLI-D-16-0620.1, 2017.

Trenberth, K. E.: The Definition of El Niño, Bull. American Meteor. Soc., 78, 2771−2777, December 1997.

Tsuda, T., Murayama, Y., Wiryosumarto, H., Harijono, S. W. B., and Kato, S.: Radiosonde observations of equatorial atmosphere dynamics over Indonesia: 1. Equatorial waves and diurnal tides, J. Geophys. Res., 99, 10491–10505, doi:10.1029/94JD00355, 1994.

Tsuda, T., Lin, X., Hayashi, H., and Noersomadi: Analysis of vertical wave number spectrum of atmospheric gravity waves in the stratosphere using COSMIC GPS radio occultation data, Atmos. Meas. Tech., 4, doi:10.5194/amt-4-1627-2011, 2011.

Wang, W., K. Matthes, T. Schmidt, and L. Neef: Recent variability of the tropical tropopause inversion layer, *Geophys. Res. Lett.*, *40*, 6308–6313, doi:10.1002/2013GL058350, 2013.

Wheeler, M. C., and Hendon, H. H.: An all-season real-time multivariate MJO index: Development of an index for monitoring and prediction, Mon. Weather Rev., 132, 1917–1932, doi:10.1175/1520-0493(2004)132<1917:AARMMI>2.0.CO;2, 2004.

Wheeler, M., and G. N. Kiladis: Convectively coupled equatorial waves: Analysis of clouds and temperature in the wavenumber–frequency domain. J. Atmos. Sci.*,* **56,** 374–399, 1999.

Wickert, J., Reigber, C., Beyerle, G., König, R., Marquardt, C., Schmidt, T., Meehan, T., Grunwaldt, L., and Galas, R.: GPS radio occultation with CHAMP: First results, Geophys. Res. Lett.,4–7, 2001.

WMO, Meteorology—A three-dimensional science, WMO Bull., 6, (Oct), 134– 138, 1957

Yadav, P., and Straus, D. M.: Circulation response to fast and slow MJO episodes, Mon. Weather. Rev., 1577–1596, doi:10.1175/MWR-D-16-0352.1, 2017.

Yoneyama K., Zhang C., Long C. N.: Tracking pulses of the Madden-Julian Oscillation. Bull. Am. Meteorol. Soc., doi:10.1175/bams-d-12-00157.1

Zeng, Z., S.-P. Ho, S. Sokolovskiy, and Y.-H. Kuo: Structural evolution of the Madden-Julian Oscillation from COSMIC radio occultation data, J. Geophys. Res., 117, D22108, doi:10.1029/2012JD017685, 2012.

Zeng, Z., Sokolovskiy, S., Schreiner, W., Hunt, D., Lin, J. and Kuo, Y. H.: Ionospheric correction of GPS radio occultation data in the troposphere, Atmos. Meas. Tech., 9, 335–346, doi:10.5194/amt-9-335-2016, 2016.

Zhang, C.: Madden Julian Oscillation, Rev. Geophys., 43(RG2003), doi:10.1029/2004RG000158, 2005.

Zhang C., Gottschalck, J., Maloney, E. D., Moncrieff, M. W., Vitart, F., Waliser, D. E., Wang, B., Wheeler, M. C.: Cracking the MJO nut. Geophys. Res. Lett., 40, 1223-1230. doi:10.1002/grl.50244, 2013.

Table 1 Radiosonde stations for daily routine balloon launches during the CINDY-DYNAMO 2011 campaign around the Maritime Continent. All stations apart from No. 2 are in Indonesia. The 'Number of profiles' column lists the number of successful balloon soundings that reached >2 km above the CPT.

No	Station name	Longitude	Latitude	Number of profiles
1	Singapore	103.80°E	1.30°N	247
2	Medan	98.68°E	3.57°N	316
3	Padang	100.35°E	0.88°S	379
4	Pangkal Pinang	106.14°E	2.16°S	253
5	Cengkareng	106.68°E	6.12°S	303
6	Ranai	108.39°E	3.91°N	240
7	Surabaya	112.78°E	7.37°S	309
8	Makassar	119.53°E	5.06°S	307
9	Palu	119.91°E	0.92°S	337
10	Manado	124.92°E	1.54°N	334
11	Ambon	128.10°E	3.71°S	312
12	Biak	136.10°E	1.19°S	321
13	Merauke	140.41°E	8.52°S	338

Table 2 Definitions of TIL sharpness and thickness

Parameter	Definition	Unit
S-aCPT	$maxN^2_{+1} - N^2$ at CPT	$\times 10^{-4}\ s^{-2}$
S-bCPT	N^2 at CPT $- minN^2_{-1}$	$\times 10^{-4}\ s^{-2}$
S-ab	$maxN^2_{+1} - minN^2_{-1}$	$\times 10^{-4}\ s^{-2}$
dH-aCPT	$Hmax - H$ of CPT	km
dH-bCPT	H of CPT $- Hmin$	km
dH-ab	$Hmax - Hmin$	km
dH	H of $80\% \times maxN^2$ above $Hmax - H$ of $80\% \times maxN^2$ below $Hmax$	km

$Hmax$: H of $maxN^2_{+1}$; $Hmin$: H of $maxN^2_{-1}$; subscript ± 1 indicates within ± 1 km
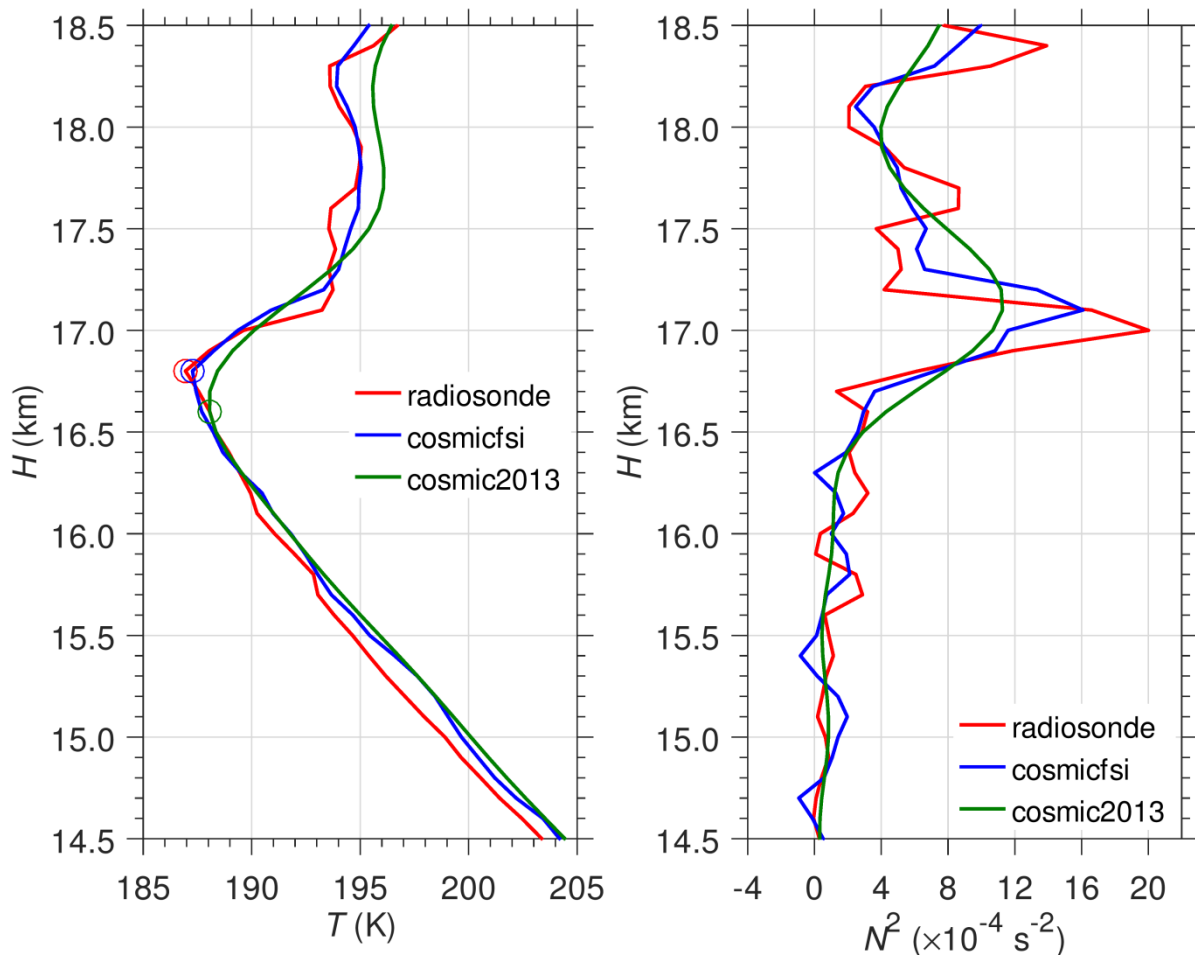
Figure 1 Typical COSMIC GPS-RO profile near the radiosonde balloon launch in Surabaya on 24 November 2011. Circles in the left panel indicate the CPT.
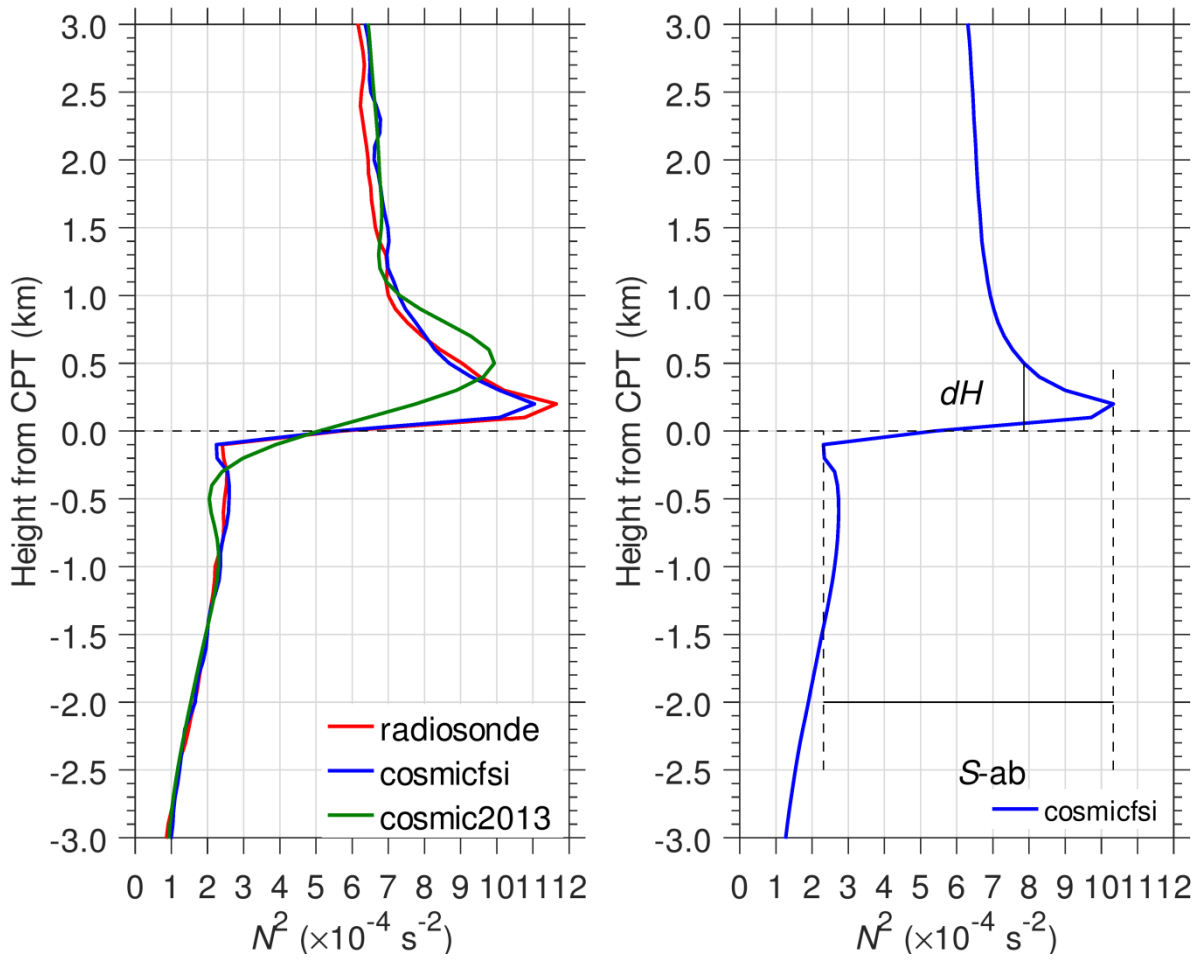
Figure 2 Mean N^2 profiles from radiosonde (red), *cosmicfsi* (blue), and *cosmic2013* (green) during CINDY-DYNAMO 2011 (left panel). Zonal mean N^2 profile in the 10°S–10°N latitude range from 10 years cosmicfsi data (right panel). All heights are relative to the CPT.
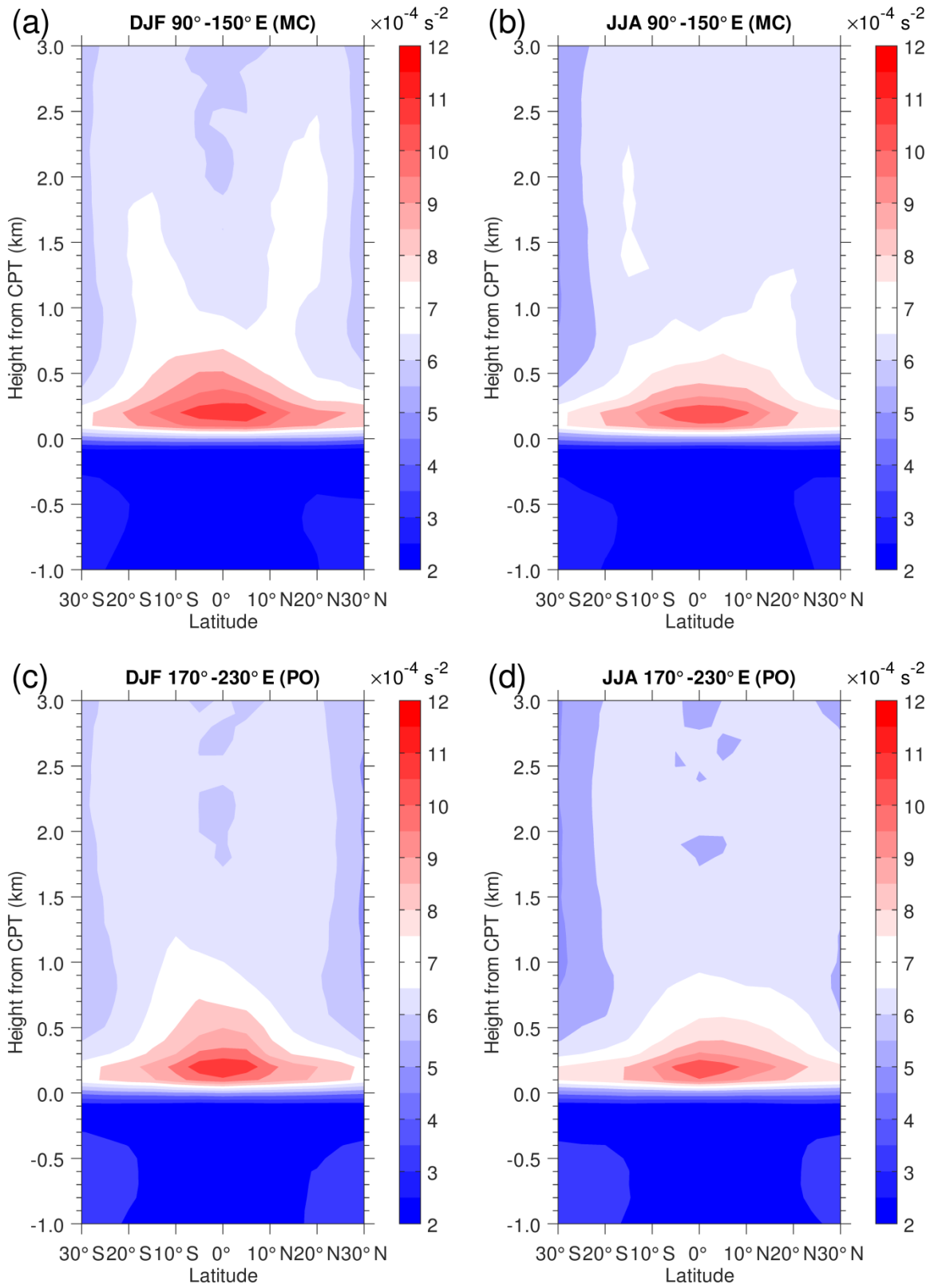
Figure 3 Height–latitude cross-sections of the mean N^2 relative to the CPT location in the vertical for (a), (c) DJF and (b), (d) JJA in the two longitude regions. Color contour interval is 0.5×10^{-4} s^{-2}.
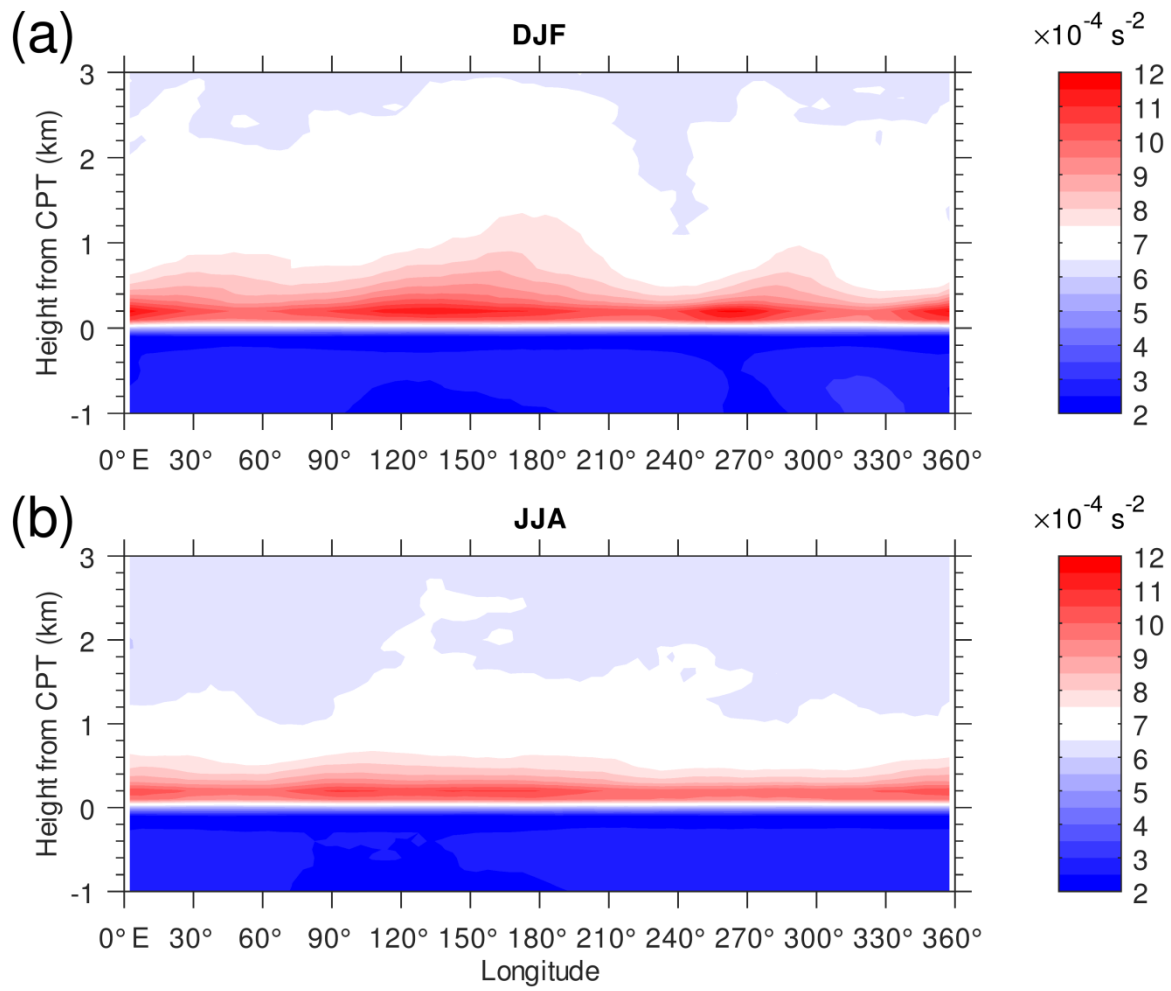
Figure 4 Height–longitude cross-sections of the mean N^2 over 10°S–10°N latitude relative to the CPT location in the vertical for (a) DJF and (b) JJA. Color contour interval is 0.5×10^{-4} s^{-2}.
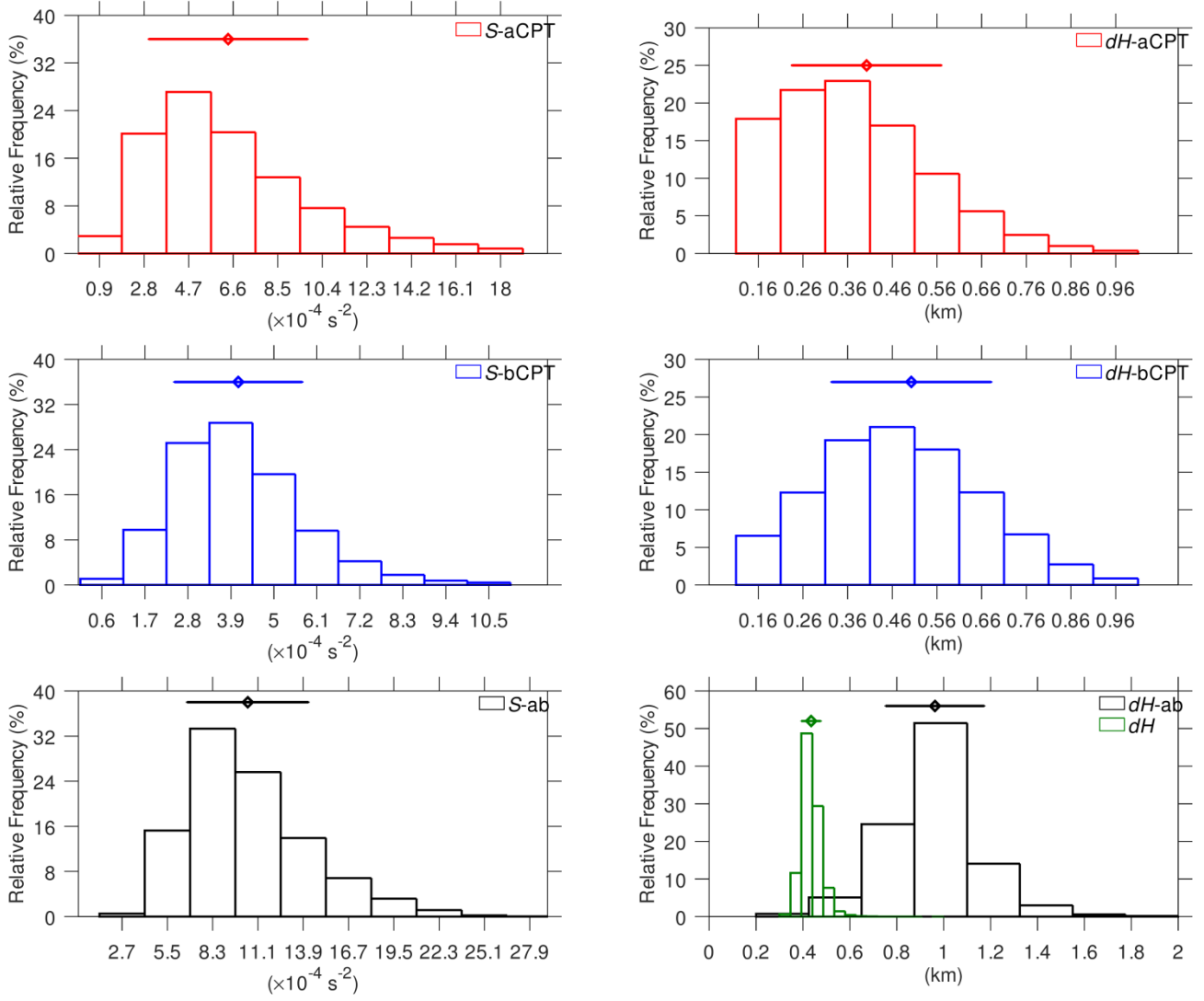
Figure 5 Frequency distribution of TIL parameters with respect to the vertical distance from the CPT. The diamond and horizontal line above each histogram represent the mean and standard deviation of each parameter, respectively.
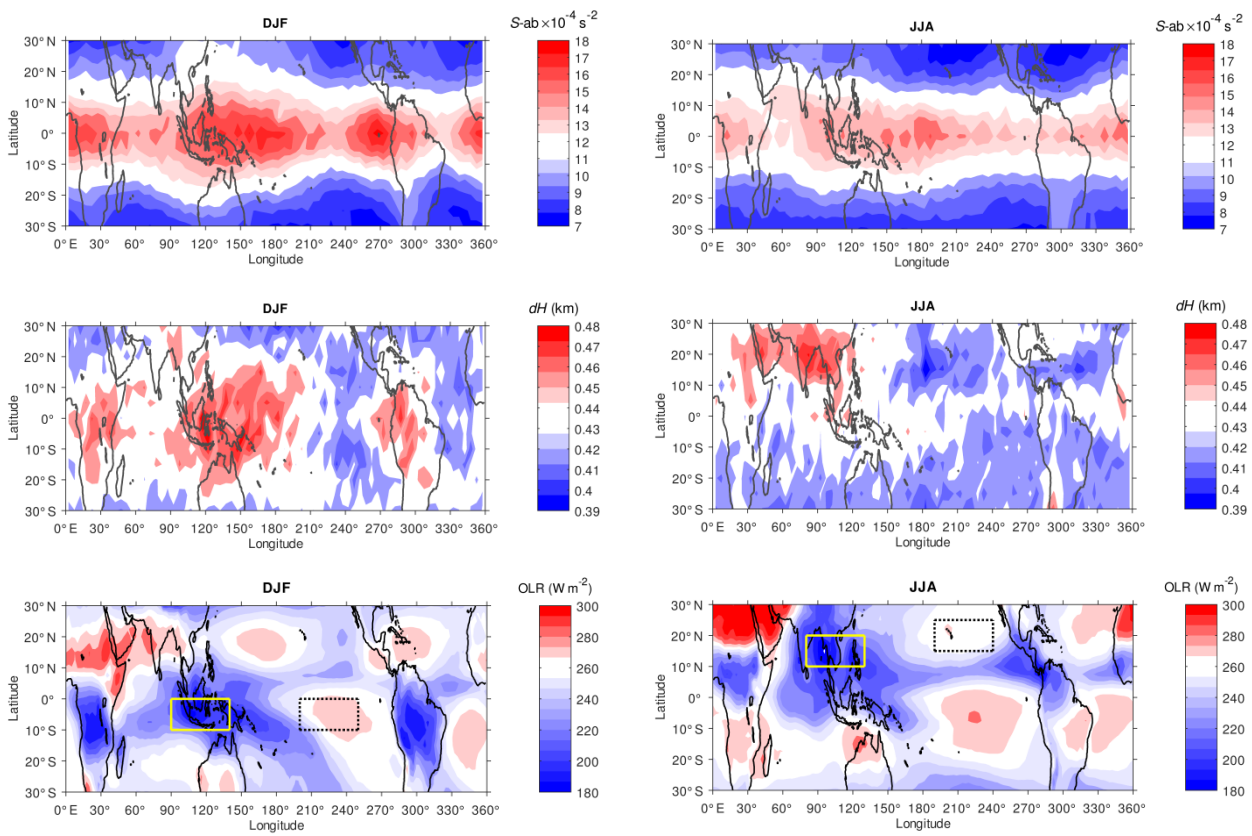
Figure 6 Horizontal distribution of the mean *S*-ab (top row), *dH* (middle row), and OLR (bottom row) during Northern Hemisphere winter (DJF) and summer (JJA). Solid-yellow and dotted-black boxes in the bottom row indicate the sample "convective" and "non-convective" regions, respectively.
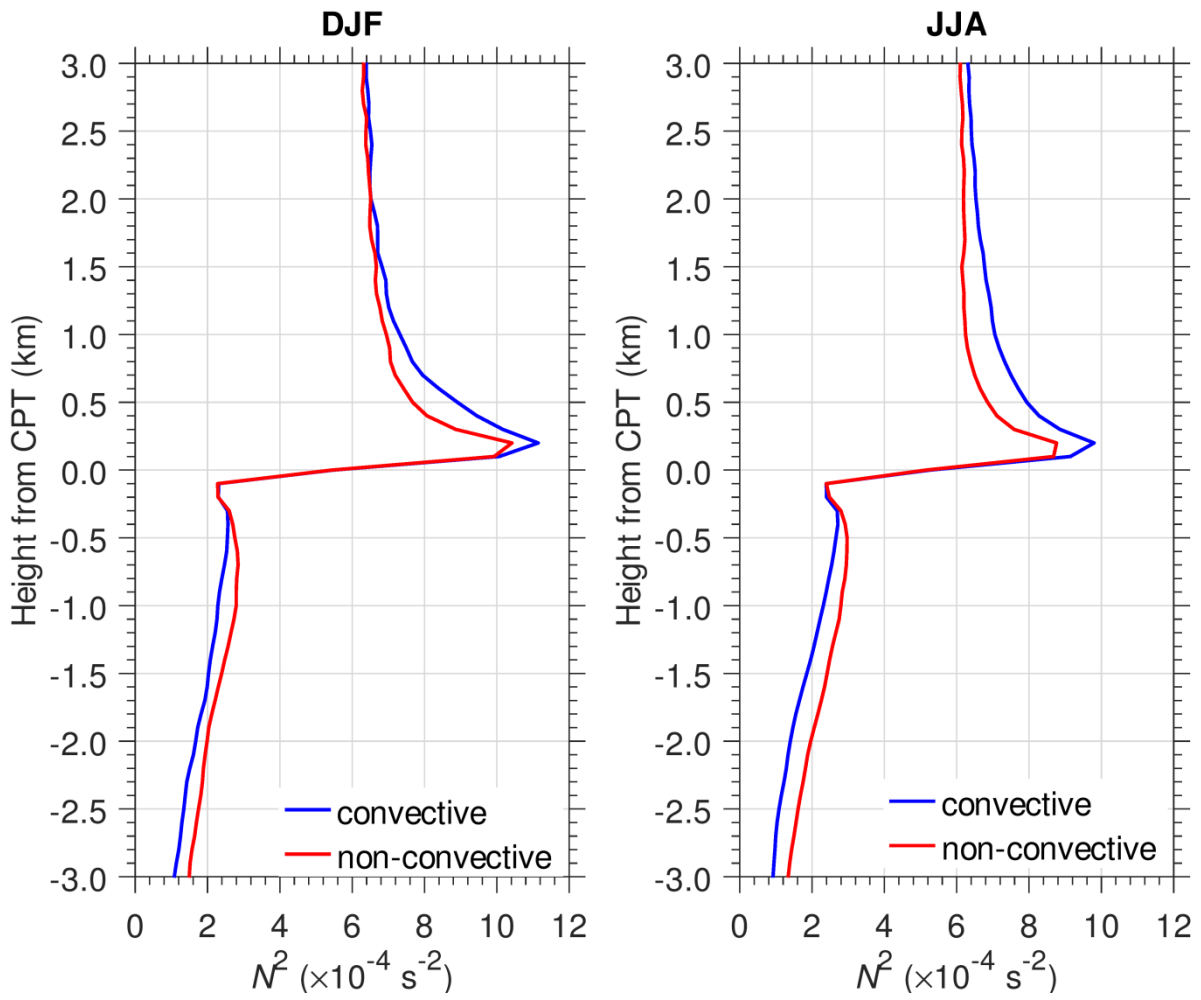
Figure 7 Mean N^2 profiles over the convective and non-convective regions defined in Fig. 10 for DJF (left) and JJA (right).
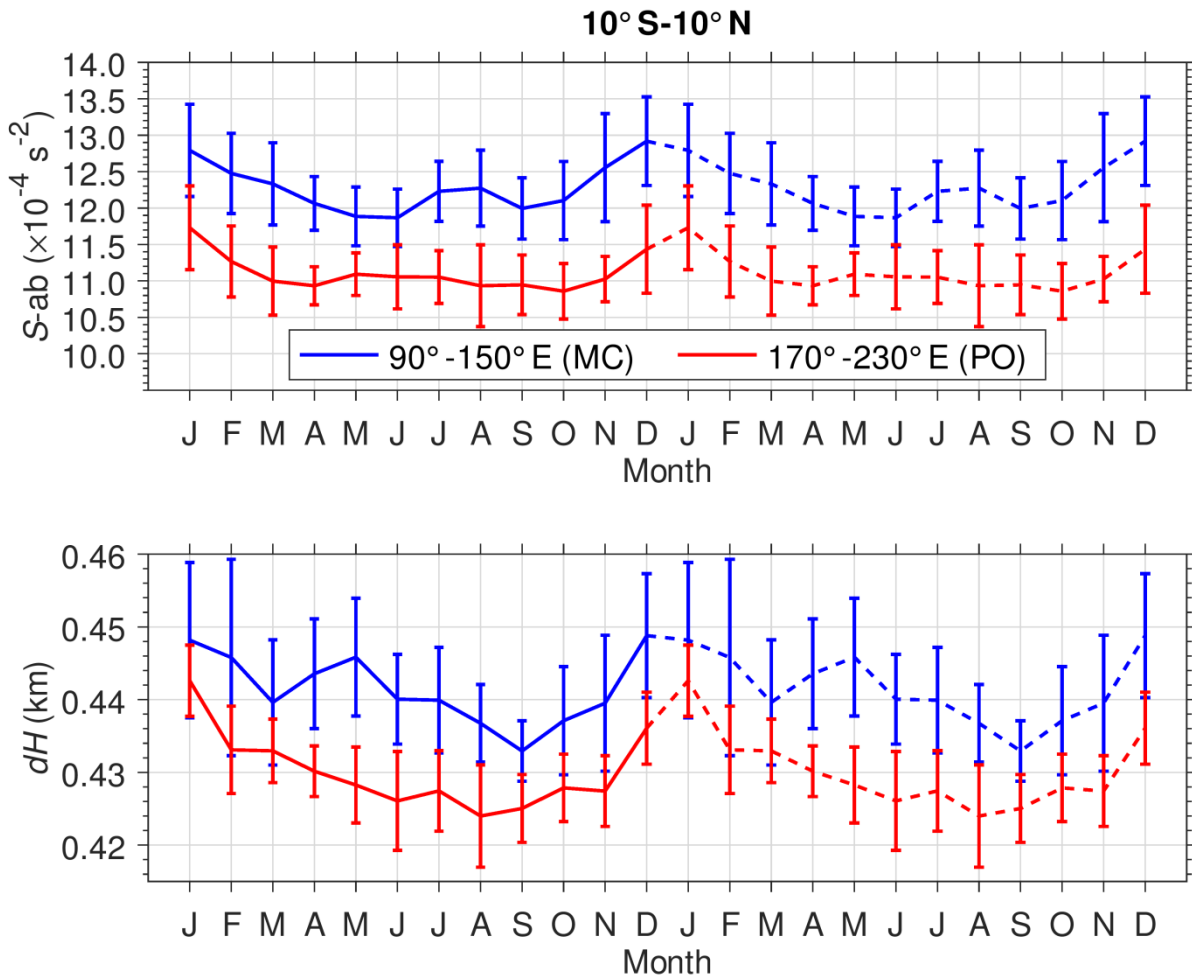
Figure 8 Seasonal variation in the mean *S*-ab (upper panel) and *dH* (lower panel) over the MC (blue line) and the PO (red line). Error bars show the standard deviation with respect to the mean value. Note that, both *S*-ab and *dH* are duplicated to show the seasonal cycle more clearly (dashed line).
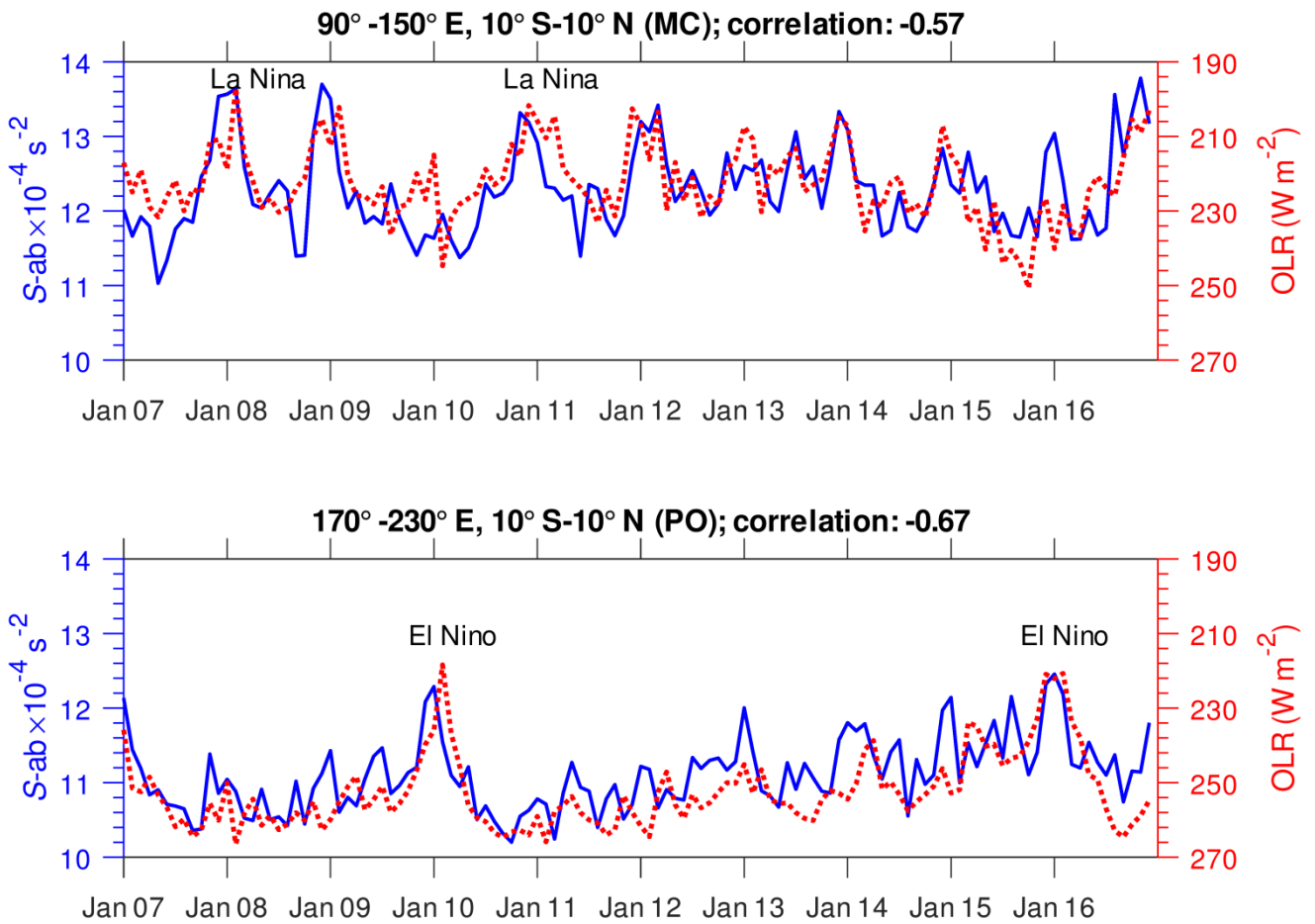
Figure 9 Time series of monthly mean *S*-ab (solid blue line) and OLR (dotted red line) for the MC (upper panel) and PO (lower panel).
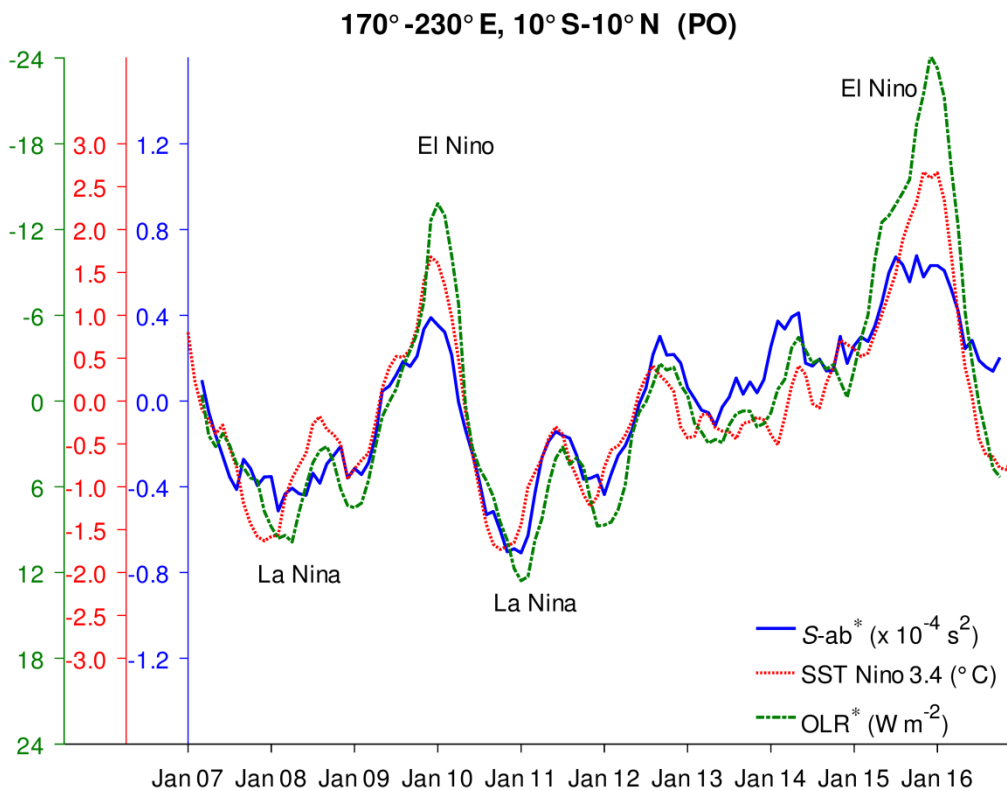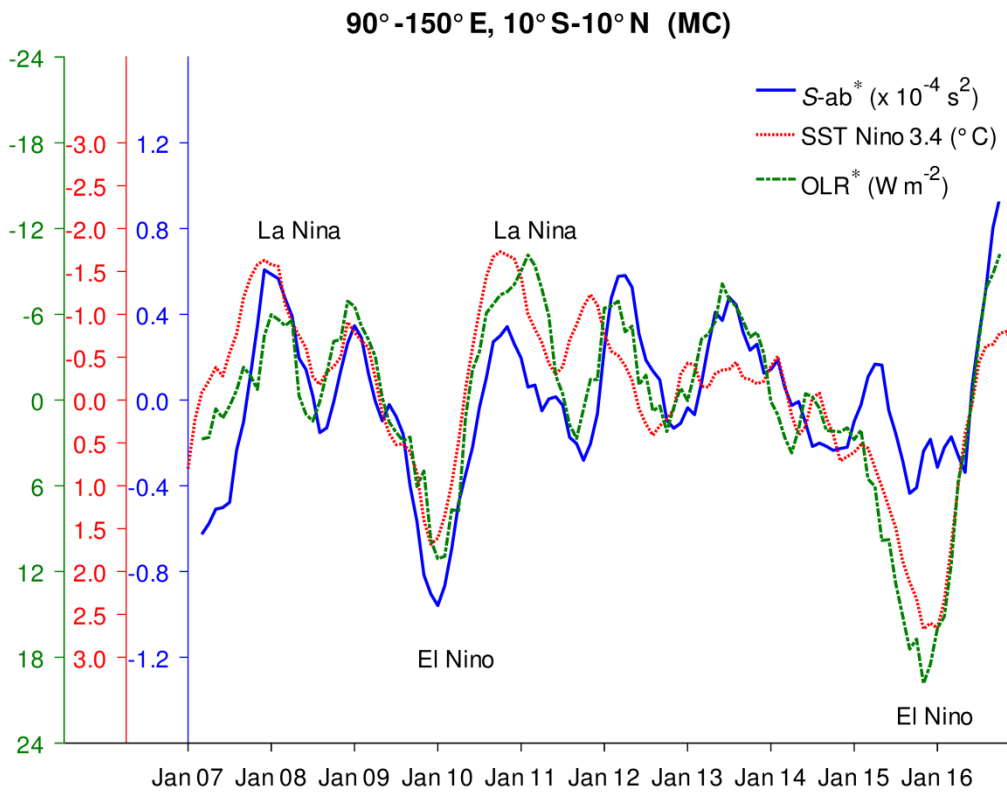
Figure 10 Interannual variations in *S*-ab anomaly (*S*-ab*) (solid blue line), OLR anomaly (OLR*) (dashed-dotted green line), and SST Nino3.4 index (dotted red line) for the MC (upper panel) and PO (lower panel). Note that the ordinate axes of both OLR* and SST Nino 3.4 index are reversed in the upper panel, but only the ordinate axis of OLR* is reversed in the lower panel.
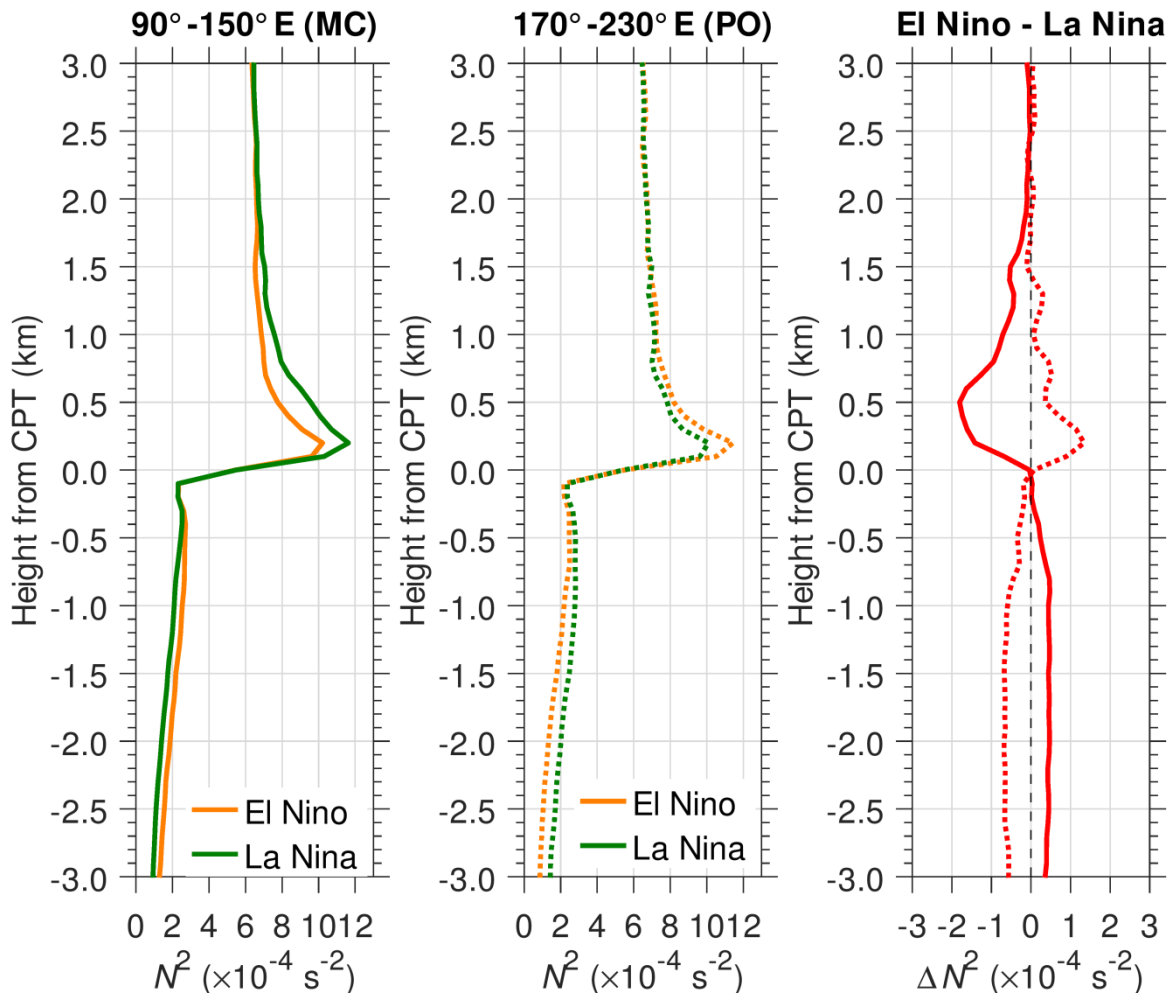
Figure 11 Mean N^2 profiles during DJF El Niño (left) and DJF La Niña (middle). Difference between the mean N^2 in DJF El-Nino and in DJF La-Nina (right) in the MC (solid line) and PO (dotted line).
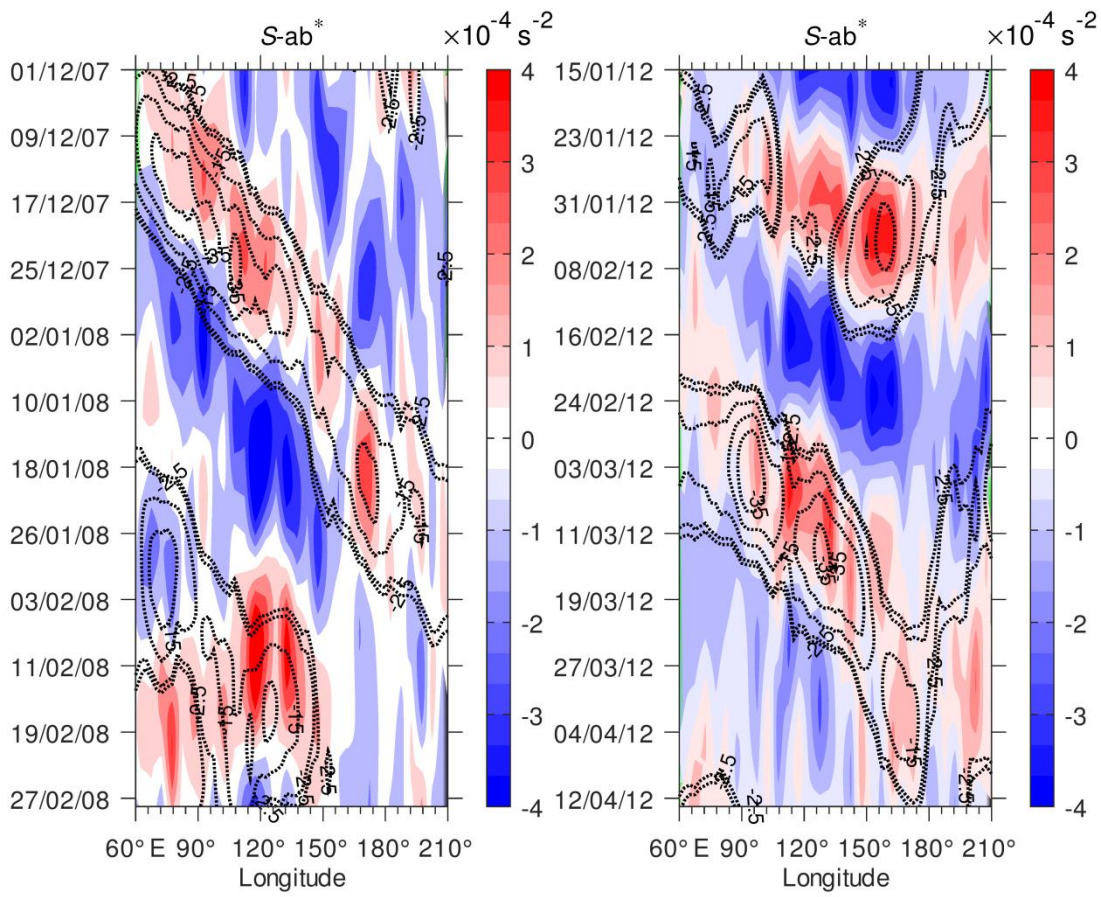
Figure 12 Time–longitude distribution (Hovmöller diagram) of S-ab* (color shading/contours) and OLR* (dotted contours). Color contour interval is 0.25×10^{-4} s^{-2} and only negative values of OLR* are shown for -35, -25, -15, -5, and -2.5 W m^{-2}.
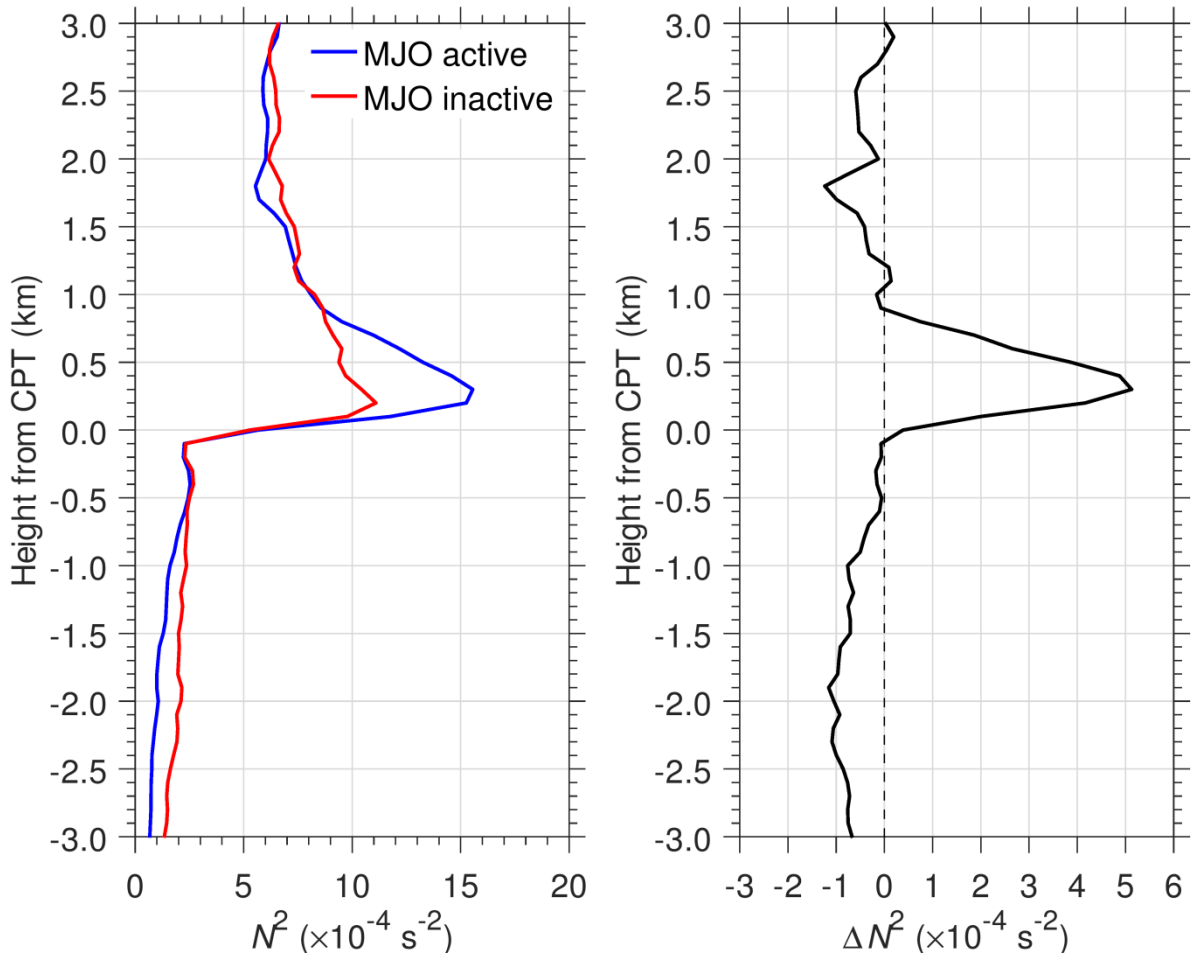
Figure 13 Mean N^2 profiles during MJO active (blue) and MJO inactive (red) phases (left) and their difference (right).
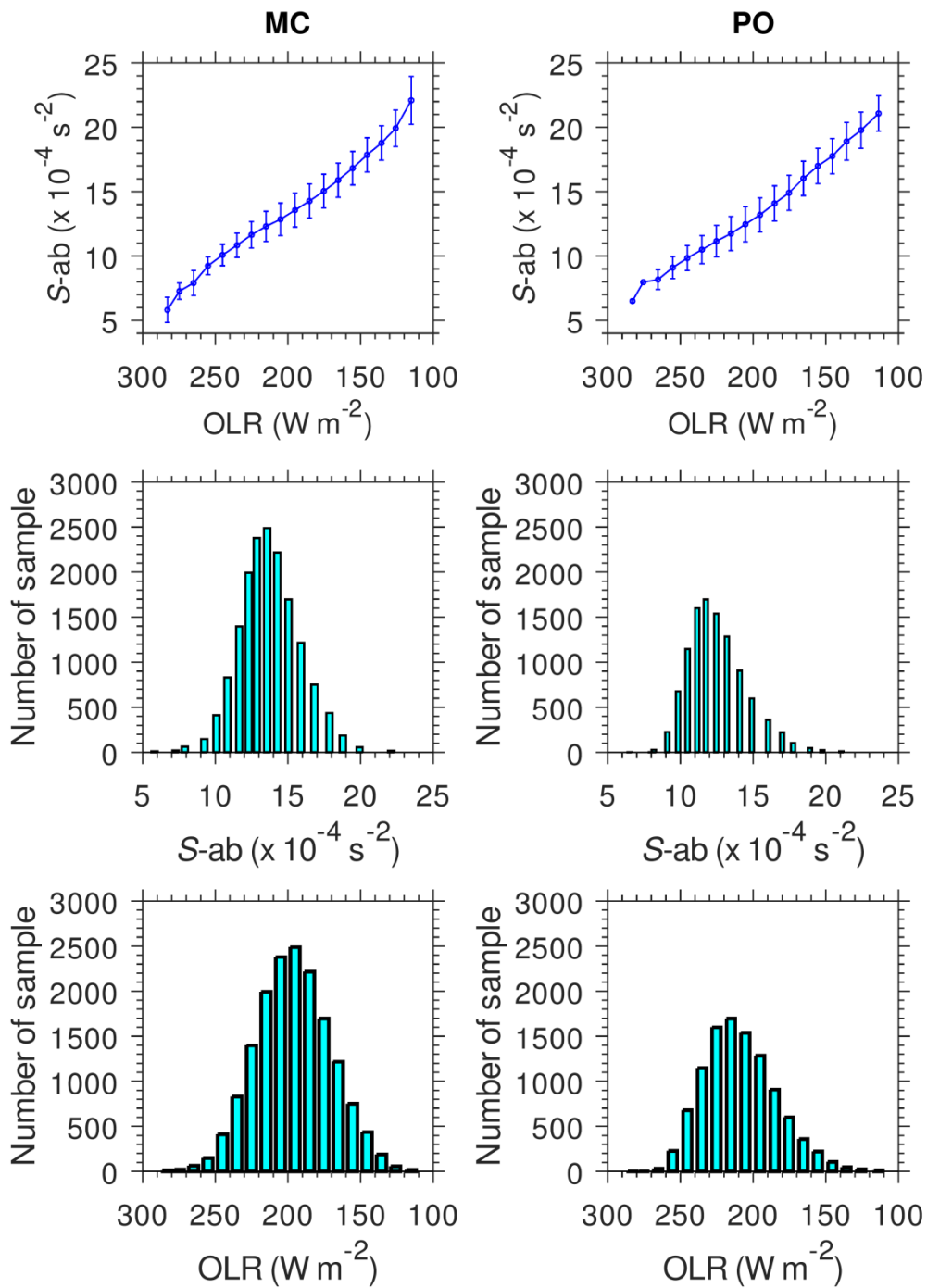
Figure 14 Diagram of *S*-ab versus OLR (top), and of the number of samples for *S*-ab and OLR (middle and bottom, respectively) in the MC (left) and PO (right) regions.